INSTITUTE OF FRACTURE AND SOLID MECHANICS

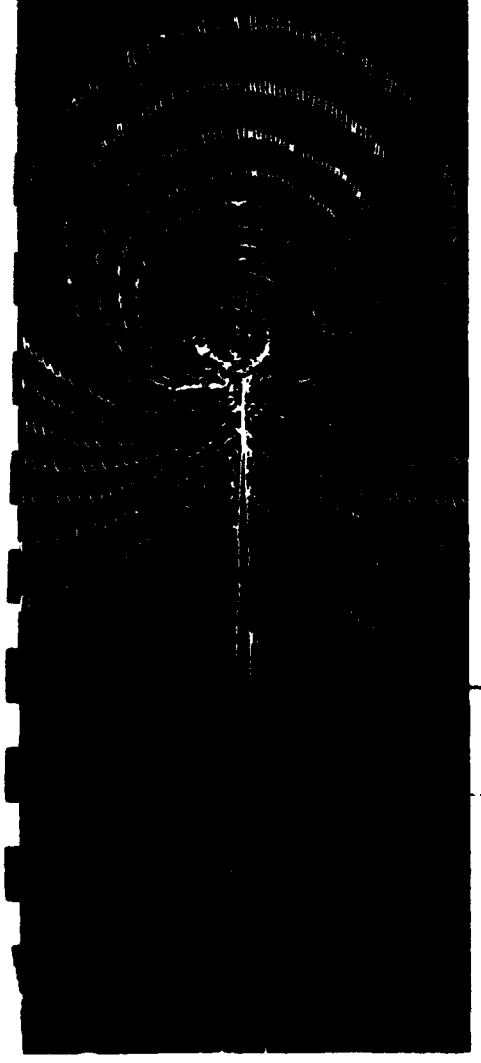

IFSM-76-76

LEHIGH UNIVERSITY

GROWTH CHARACTERISTICS OF A THROUGH CRACK IN A PLATE SPECIMEN

BY

P. D. HILTON
G. C. SIH
B. V. KIEFER

TECHNICAL REPORT
AUGUST 1976

DEPARTMENT OF THE NAVY
OFFICE OF NAVAL RESEARCH
ARLINGTON, VIRGINIA 22217

GROWTH CHARACTERISTICS OF A THROUGH CRACK IN A PLATE SPECIMEN

by

P. D. Hilton
G. C. Sih
B. V. Kiefer

LEHIGH UNIVERSITY
Institute of Fracture and Solid Mechanics
Bethlehem, Pennsylvania 18015

August 1976

Technical Report
Prepared under Contract N00014-76-C-0094
for
Department of the Navy
Office of Naval Research
Arlington, Virginia 22217

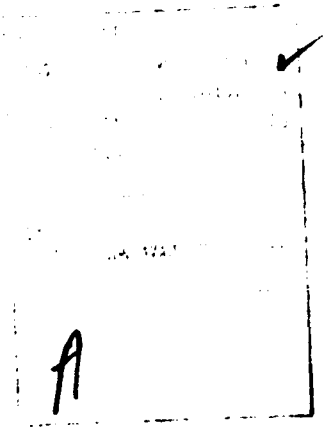

ABSTRACT

This report describes the results of a theoretical study of the problem of a through crack in a tensile plate specimen. Experimental observations indicate that the crack front grows stably in the specimen interior forming a "thumb nail" shape prior to unstable fracture. The amount of interior growth before fracture is found to depend on both geometry (relative specimen thickness), the material properties, and the amount of yielding which tends to delay the onset of rapid fracture.

The goal of this work is to study the interaction of material nonlinearity with geometry and their combined effect on the fracture process. To this end, two-dimensional elastic-plastic and three-dimensional elastic calculations have been performed. The finite element method, specialized to crack problems, is the tool used to obtain numerical results. Predictions on the increments of growth along the crack front are made on the basis of the strain energy density theory that assumes crack trajectory to coincide with path of minimum strain energy density function. Related three-dimensional elastic-plastic calculations are currently being developed to complete the modeling of the ductile fracture process in plate specimens.

TWO-DIMENSIONAL ELASTIC-PLASTIC ANALYSIS OF LONG CRACKS

A. Introduction

The behavior of a center crack specimen containing a long crack and correspondingly short ligament is considered. Experimental observations of crack growth through the last ligament to the specimen surface indicate that the crack turns away from its initial direction and final failure occurs at an angle to the original crack plane, Figure 1. This change of direction may be either clockwise or counterclockwise and the choice is believed to depend on a small nonalignment of the crack with the mid-plane of loading not treated in the analysis.

A similar phenomenon is observed in the fracture of moderately thick specimens where the combinations of material properties (yield stress) and specimen geometry violate the ASTM requirements for K_{1c} testing [1]. Here, the crack grows in the plane of the initial crack configuration in the specimen interior but deviates from that plane near the specimen surfaces forming "shear lips". A three-dimensional description of the fracture sequence is pertinent. The crack grows stably from its initial configuration in a planar fashion developing a curved crack front as shown in Figure 2. The point of instability and the breakthrough of the curved crack front to the plate surfaces (at an angle to the plane of the main crack) appear to occur at about the same point in the loading history. Again, local conditions are assumed to de-

termine whether the shear lip will form on one crack surface or the other.

The authors hypothesize that crack turning upon approaching a specimen surface in the cases of (a) the "last" ligament of fracture and (b) the formation of shear lips are different manifestations of the same phenomenon. Further, the understanding of the process involved in the formation of shear lips is fundamental to the prediction of the stable-unstable transition in fracture. That problem is of considerable interest to the authors; however, it is difficult and complex to manage because it requires three-dimensional elastic-plastic analysis for a specimen containing a growing crack. Therefore, the phenomenon of crack turning during the "last" ligament of growth is studied here using two-dimensional analysis to gain insight into the shear lip formation process.

B. Stress Analysis

A two-dimensional finite element computer program developed in [2,3] is employed to carry out the stress analysis. The program is based on the twelve node isoparametric element. It includes a specialized crack tip element which enforces the Hutchinson-Rice plastic singularity solution [4]. The singularity solution, and therefore the finite element program, is based on a power hardening model of material behavior and the J_2 deformation theory of plasticity, i.e., the strain-stress relationship is expressed in the form

$$e_{ij} = \frac{1+\nu}{E} s_{ij} + \frac{3}{2} \frac{\alpha}{E} \left[\left(\frac{\sigma_e}{\sigma_{yd}} \right)^{n-1} - \frac{\sigma_{yd}}{\sigma_e} \right] s_{ij}$$

$$\varepsilon_{pp} = \frac{1-2\nu}{E} \sigma_{pp} \tag{1}$$

where $e_{ij} = \varepsilon_{ij} - \frac{1}{3} \varepsilon_{pp} \delta_{ij}$ is the strain deviation and the stress deviation is $s_{ij} = \sigma_{ij} - \frac{1}{3} \sigma_{pp} \delta_{ij}$. The Hutchinson-Rice plane strain solution for the asymptotic stress, strain, and displacement (relative to the crack tip) fields respectively takes the form:

$$\sigma_{ij} = \sigma_{yd} K r^{-\frac{1}{n+1}} \tilde{\sigma}_{ij}(\theta)$$

$$\varepsilon_{ij} = \frac{\alpha}{E} \sigma_{yd} K^n r^{-\frac{1}{n+1}} \tilde{\varepsilon}_{ij}(\theta) \tag{2}$$

$$u_i = \frac{\alpha}{E} \sigma_{yd} K^n r^{\frac{1}{n+1}} \tilde{u}_i(\theta)$$

where (r,θ) represent a polar coordinate system centered at the crack tip and where the plastic intensity factor K depends on global geometry and loading conditions.

The crack tip element is semi-circular in shape and its displacement shape function is

$$u_x = u_{x_o} + K_\varepsilon \left[\frac{\alpha}{E} \sigma_{yd} r^{\frac{1}{n+1}} \tilde{u}_x(\theta) \right]$$

$$u_y = K_\varepsilon \left[\frac{\alpha}{E} \sigma_{yd} r^{\frac{1}{n+1}} \tilde{u}_y(\theta) \right] \tag{3}$$

where u_{x_o} and K_ε are the generalized nodal displacement component and $K_\varepsilon = K^n$.

C. Results

The center crack specimen is considered with two width to length ratios: 4:2 as employed in the previous report [5] and 4:4. Table 1 shows the crack lengths and applied loads, σ_o, which were treated.

TABLE 1 - APPLIED STRESS TO YIELD STRESS RATIO FOR DIFFERENT SIZE SPECIMENS

	Width	Length	Crack Length	σ_o/σ_{yd}
1	4"	2"	3.2"	0.28
2	↓	↓	↓	0.31
3	↓	↓	↓	0.35
4	↓	↓	↓	0.38
5	4"	4"	2.4"	0.28
6	↓	↓	↓	0.313
7	↓	↓	↓	0.356
8	↓	↓	↓	0.38
9	4"	4"	3.2"	0.28
10	↓	↓	↓	0.30
11	↓	↓	↓	0.32
12	↓	↓	↓	0.34
13	↓	↓	↓	0.36
14	↓	↓	↓	0.38
15	4"	4"	3.6"	0.28
16	↓	↓	↓	0.313
17	↓	↓	↓	0.38

The values of the material parameters chosen for these calculations are:

$E = 1.0$, $\nu = 0.3$

$\sigma_{yd} = 1.0$, $a = 0.5$ and $n = 5.0$

Figure 3 shows a uniaxial tensile stress-strain curve for this material model. Typical grid patterns for the two aspect ratios are shown in Figures 4 and 5. Figures 6 to 22 show the regions in each specimen which have yielded, i.e., the circled dots represent quadrature points at which the applied stress is greater than the yield stress. Also included in these figures is a curved line from the crack tip to the specimen boundary. This line represents the numerical result for the minimum strain energy density path along which the crack is assumed to follow.

D. Discussion

In carrying out these computations, the authors were particularly interested in obtaining information about the plastic region between the crack tip and the specimen boundary in order to get insight into the shear lip problem. The results obtained indicate that in every case there exists an elastic zone between the crack tip and the boundary. However, for the width to length ratio of 4:2, a secondary plastic zone is observed to form at the free boundary. This secondary plastic zone is absent from the results with specimen width to length ratio of

4:4. These results emphasize the importance of geometry on stress field and therefore crack propagation.

The pertinent question is whether the crack would run through the region of maximum plastic deformation toward the specimen boundary or if it would attempt to avoid the deformed material, growing into the elastic zone in front of the tip and then diverging from the line of symmetry to break through the last ligament at an angle. The paths of minimum strain energy density consistently lie between the region of maximum plastic deformation and the horizontal axis (connecting the crack tip to the free surface). Thus, the strain energy density theory predicts that the crack will propagate close to the inner elastic-plastic boundary intersecting the surface at an oblique angle. Careful experimental measurements are needed to confirm the accuracy of this prediction.

Three-dimensional elastic-plastic analysis for a specimen with a curved crack front is underway to examine the similarity of the shear lip breakthrough phenomenon with the two-dimensional "last ligament" problem.

THREE-DIMENSIONAL ELASTIC ANALYSIS AND GROWTH PREDICTIONS

A three-dimensional element which incorporates the elastic crack front singularity and is applicable to curved, as well as straight, crack fronts is formulated. A number of calculations are performed to establish the accuracy of results which can be anticipated using the specialized elements in conjunction with isoparametric elements. Then the finite element procedure is employed together with a strain energy density based criterion to predict increments of crack growth.

A. Formulation of a Specialized Finite Element Procedure for Three-Dimensional Crack Problems

The finite element displacement method incorporating isoparametric elements [6] will be employed. In general, an element is enclosed by six surfaces with nodal points chosen along the element edges (a five surface element will be introduced later in the text). A coordinate transformation is employed to map the element into a cube, Figure 23. The inverse mapping function can be expressed in the form

$$\begin{bmatrix} x \\ y \\ z \end{bmatrix} = \sum_i N_i(p,s,t) \begin{bmatrix} x_i \\ y_i \\ z_i \end{bmatrix} \qquad (4)$$

where $i = 1$, the number of nodes associated with the element, and (x_i, y_i, z_i) are the coordinates of the ith node. The func-

tions $N_i(p,s,t)$ associated with the mapping are polynomial functions with the property

$$N_i(p,s,t) = \begin{cases} 1 \text{ for } p,s,t = p_i,s_i,t_i & \text{(the point in the mapped shape which corresponds to } x_i, y_i, z_i) \\ 0 \text{ for } p,s,t = p_j,s_j,t_j & j \neq i \end{cases} \tag{5}$$

The same functions $N_i(p,s,t)$ are used in the approximation for the displacement field within the element, i.e., the interior displacement components are expressed in terms of the corresponding nodal components as

$$\begin{bmatrix} u_x \\ u_y \\ u_z \end{bmatrix} = \sum_i N_i(p,s,t) \begin{bmatrix} u_{x_i} \\ u_{y_i} \\ u_{z_i} \end{bmatrix} \tag{6}$$

These functions $N_i(p,s,t)$ are termed as "displacement shape functions".

The strains components are obtained in terms of the nodal displacement components by differentiating equation (6), i.e.,

$$\varepsilon_x = \sum_i \frac{\partial N_i}{\partial x} u_{x_i} \qquad \gamma_{xy} = \sum_i \frac{\partial N_i}{\partial y} u_{x_i} + \sum_i \frac{\partial N_i}{\partial x} u_{y_i}$$

$$\varepsilon_y = \sum_i \frac{\partial N_i}{\partial y} u_{y_i} \qquad \gamma_{yz} = \sum_i \frac{\partial N_i}{\partial z} u_{y_i} + \sum_i \frac{\partial N_i}{\partial y} u_{z_i}$$

$$\varepsilon_z = \sum_i \frac{\partial N_i}{\partial z} u_{z_i} \qquad \gamma_{zx} = \sum_i \frac{\partial N_i}{\partial x} u_{z_i} + \sum_i \frac{\partial N_i}{\partial z} u_{x_i} \tag{7}$$

where the Jacobian of the transformation

$$\begin{bmatrix} \frac{\partial N_i}{\partial p} \\ \frac{\partial N_i}{\partial s} \\ \frac{\partial N_i}{\partial t} \end{bmatrix} = \begin{bmatrix} \frac{\partial x}{\partial p} & \frac{\partial y}{\partial p} & \frac{\partial z}{\partial p} \\ \frac{\partial x}{\partial s} & \frac{\partial y}{\partial s} & \frac{\partial z}{\partial s} \\ \frac{\partial x}{\partial t} & \frac{\partial y}{\partial t} & \frac{\partial z}{\partial t} \end{bmatrix} \begin{bmatrix} \frac{\partial N_i}{\partial x} \\ \frac{\partial N_i}{\partial y} \\ \frac{\partial N_i}{\partial z} \end{bmatrix} \tag{8}$$

is inverted to obtain the needed partial derivatives. The result is expressed symbolically as

$$\vec{\varepsilon} = [B]\, \vec{\delta} \tag{9}$$

where

$$\vec{\varepsilon} = (\varepsilon_x, \varepsilon_y, \varepsilon_z, \gamma_{xy}, \gamma_{yz}, \gamma_{zx})$$

$$\vec{\delta} = (u_{x_1}, u_{y_1}, u_{z_1}, u_{x_2}, \ldots u_{z_n}) \tag{10}$$

n = number of nodes per element

The stress components are related to the strain components through the generalized Hooke's law

$$\vec{\sigma} = [D]\,\vec{\varepsilon} \tag{11}$$

The strain energy in an element can then be expressed in the form

$$W = \frac{1}{2}\,\vec{\delta}^{T}\,[k]\,\vec{\delta} \tag{12}$$

where [k] is the element stiffness matrix given by

$$[k] = \int_{-1}^{1}\int_{-1}^{1}\int_{-1}^{1} [B]^{T}\,[D][B]\,\det J\; dp\,ds\,dt \tag{13}$$

and where detJ is the determinate of the Jacobian for the transformations given in equation (8).

The potential energy of the body, calculated as the sum of the element strain energy contributions minus the work done by applied forces, is minimized with respect to nodal displacement components to obtain a set of linear algebraic equations for the determination of their values.

Specialized "singular" elements are developed to properly model the crack front singularity. The approximate form for the displacement field within elements adjacent to the crack edge is chosen to include the first term of the asymptotic solution

$$u_x = \frac{(1+\nu)}{4E} k_1(z)\sqrt{2r}\,[(5-8\nu)\cos\frac{\theta}{2} - \cos\frac{3\theta}{2}] + O(r)$$

$$= k_1(z)\,\tilde{u}_x(r,\theta) + O(r)$$

$$u_y = \frac{(1+\nu)}{4E} k_1(z)\sqrt{2r}\,[(7-8\nu)\sin\frac{\theta}{2} - \sin\frac{3\theta}{2}] + O(r) \qquad (14)$$

$$= k_1(z)\,\tilde{u}_y(r,\theta) + O(r)$$

$$u_z = O(r) \text{ as } r \to 0$$

where E is Young's modulus and ν is Poisson's ratio.

Here, (r,θ,z) are local cylindrical coordinates centered on the crack front with z tangent to the crack edge. The geometry of these singular elements is designed to follow the local cylindrical coordinate system in which the singular solution is given. A typical singular element configuration is shown in Figure 24. Its cross section in the plane normal to the crack edge is pie shaped. These singular elements are then arranged to fill a volume with circular cross section centered on the crack edge, Figure 25.

The assumed form for the displacement field within each of the singular elements consists of two parts. It contains the standard isoparametric element approximation to the displacement field plus a contribution from the elastic singular solution. In order that this displacement field matches that

of standard isoparametric elements at nodes common to both elements, the contribution from the singularity solution is forced to vanish at these nodes. The resulting displacement field can be written using local coordinates (x,y,z) along the crack front in the form

$$u_x(p,s,t) = \sum N_i(p,s,t)u_{x_i} + k_1(z)[\tilde{u}_x(r,\theta) - \sum \tilde{u}_y(r_i,\theta_i)N_i(p,s,t)]$$

$$u_y(p,s,t) = \sum N_i(p,s,t)u_{y_i} + k_1(z)[\tilde{u}_y(r,\theta) - \sum \tilde{u}_y(r_i,\theta_i)N_i(p,s,t)] \qquad (15)$$

$$u_z(p,s,t) = \sum N_i(p,s,t)u_{z_i}$$

where $\tilde{u}_z(r,\theta)$ and $\tilde{u}_y(r,\theta)$ are given by equation (14).

The variation of the stress intensity factor along the crack front is approximated in a piece-wise manner consistent with the finite element displacement approximations, i.e.,

$$k_1(z) = \sum_i N_i^*(s)k_i \qquad (16)$$

where s is the variable in the mapped space which corresponds to z and where the summation is over nodes adjacent to the element along the crack edge. The shape functions $N_i^*(s)$ are given by $N_i^*(s) = N_i(-1,s,-1)$.

Transforming to the global coordinate system (X,Y,Z), the assumed form for the displacement field in a singular element becomes

$$
\begin{aligned}
u_X &= \sum_i N_i(p,s,t)u_{X_i} + \sum_i \{N_i^*(s)[\tilde{u}_x(r,\theta)\cos\alpha \\
&\quad - \sum_j N_j(p,s,t)\tilde{u}_x(r_j,\theta_j)\cos\alpha_j]\}k_i \\
u_Y &= \sum_i N_i(p,s,t)u_{Y_i} + \sum_i \{N_i^*(s)[\tilde{u}_y(r,\theta) \\
&\quad - \sum_j N_i(p,s,t)\tilde{u}_y(r_j,\theta_j)]\}k_i \\
u_Z &= \sum_i N_i(p,s,t)u_{Z_i} + \sum_i \{N_i^*(s)[\tilde{u}_x(r,\theta)\sin\alpha \\
&\quad - \sum_j N_j(p,s,t)\tilde{u}_x(r_j,\theta_j)\sin\alpha_j]\}k_i
\end{aligned}
\tag{17}
$$

where α is the angle between the normal to the crack edge (in the plane of the crack front) and the x axis given by $\alpha = \arctan\left(-\frac{\partial X/\partial s}{\partial Z/\partial s}\right)$.

The strain components are obtained by differentiating the displacement expressions in equation (17) as:

$$
\begin{aligned}
\epsilon_X &= \sum_i N_{i,X}u_{X_i} + \sum_i \{N_i^*\,[\tilde{\epsilon}_x\cos^2\alpha - \tilde{u}_x\frac{\partial\cos\alpha}{\partial z}\sin\alpha \\
&\quad - \sum_j N_{j,X}\tilde{u}_{x_j}\cos\alpha_j] - \sum_i N_{i,z}^*\sin\alpha\,[\tilde{u}_x\cos\alpha \\
&\quad - \sum_j N_j\tilde{u}_{x_j}\cos\alpha_j]\}k_i
\end{aligned}
$$

$$\varepsilon_Y = \sum_i N_{i,Y} u_{Y_i} + \sum_i N_i^* [\tilde{\varepsilon}_y - \sum_j N_{j,Y} \tilde{u}_{y_j}] k_i$$

$$\varepsilon_Z = \sum_i N_{i,Z} u_{Z_i} + \sum_i \{N_i^* [\tilde{\varepsilon}_x \sin^2\alpha + \tilde{u}_x \frac{\partial \sin\alpha}{\partial z} \cos\alpha$$

$$- \sum_j N_{j,Z} \tilde{u}_{x_j} \sin\alpha_j] + \sum_i N_{i,z}^* \cos\alpha [\tilde{u}_x \sin\alpha$$

$$- \sum_j N_j \tilde{u}_{x_j} \sin\alpha_j]\} k_i$$

$$\gamma_{XY} = \sum_i (N_{i,X} u_{Y_i} + N_{i,Y} u_{X_i}) + \sum_i \{N_i^* [\tilde{\gamma}_{xy} \cos\alpha$$

$$- \sum_j N_{j,Y} \tilde{u}_{x_j} \cos\alpha_j - \sum_j N_{j,X} \tilde{u}_{y_j}] - N_{i,z}^* \sin\alpha (\tilde{u}_y$$

$$- \sum N_j \tilde{u}_{y_i})\} k_i \qquad (18)$$

$$\gamma_{YZ} = \sum_i (N_{i,Y} u_{Z_i} + N_{i,Z} u_{Y_i}) + \sum_i \{N_i^* [\tilde{\gamma}_{xy} \sin\alpha$$

$$- \sum N_{j,Y} \tilde{u}_{y_j}] + N_{i,z}^* \sin\alpha (\tilde{u}_y - \sum N_j \tilde{u}_{y_j})\} k_i$$

$$\gamma_{ZX} = \sum_i (N_{i,Z} u_{X_i} + N_{i,X} u_{Z_i}) + \sum_i \{N_i^* [\tilde{\varepsilon}_x \sin 2\alpha$$

$$+ \tilde{u}_x (\frac{\partial \cos\alpha}{\partial z} \cos\alpha - \frac{\partial \sin\alpha}{\partial z} \sin\alpha) - \sum_j N_{j,Z} \cos\alpha_j \tilde{u}_{x_j}$$

$$- \sum_j N_{i,X} \tilde{u}_{x_j} \sin\alpha_j] + N_{i,z}^* [\cos\alpha (\tilde{u}_x \cos\alpha$$

$$- \sum_j N_j \tilde{u}_{x_j} \cos\alpha_j) - \sin\alpha (\tilde{u}_x \sin\alpha - \sum_j N_j \tilde{u}_{x_j} \sin\alpha_j)]\} k_i$$

This approximation to the strain field, used in the elements adjacent to the crack edge, contains the elastic strain singularity plus non-singular contributions associated with standard isoparametric elements. The nodal values of the stress intensity factors can now be treated as generalized nodal displacement components or degrees of freedom to be determined through the finite element procedure. Let $\vec{\delta}^*$ be a vector representation of the degrees of freedom associated with a singular element, then

$$\vec{\delta}^* = u_{X_1}, u_{Y_1}, u_{Z_1}, u_{X_2}, \ldots, u_{Z_m}, k_1, k_2, \ldots, k_n$$

where m is the number of nodes of the element and n is the number of these nodes which lie along the crack edge. Then the approximation to the strain components in a singular element can be expressed in the same form as that employed for a standard element, i.e.,

$$\vec{\varepsilon} = [B^*] \vec{\delta}^* \tag{19}$$

and the corresponding element stiffness matrix is given as

$$[k] = \int_{-1}^{1} \int_{-1}^{1} \int_{-1}^{1} [B^*]^T [D] [B^*] \det J \, dp\,ds\,dt \tag{20}$$

B. Remarks on Accuracy - Straight Crack Front Results

The specified finite element procedure described above has

been employed to solve the problem of a center crack (straight crack front) specimen under uniform tensile loading. Results were obtained for two specimen thicknesses in order to study the influence of specimen thickness on the through-the-thickness variation of the near edge fields. Initial results were based on the grid patterns shown in Figure 25. (The crack edge was taken as straight with a singular element radius of 0.25 or 1/16th of the half crack length. The corresponding curves for the variation of the normalized stress intensity factor $(\frac{k_1}{\sigma_o\sqrt{a}})$ with the normalized transverse coordinate (z/h) are given in Figure 26. The results shown in this figure are for the case where the stress intensity factor is constrained to be zero at the free surface. Note the expected trend, i.e., as the plate thickness h is decreased relative to the in-plane dimensions, the degree of variation of the stress intensity factor increases. (For an infinitely thick plate, the stress intensity factor is constant at the plane strain value).

These calculations have been repeated using a significantly smaller singular element radius, i.e., r_o = 0.05 or 1/40 of the half crack length. The curves for $\frac{k_1}{\sigma_o\sqrt{a}}$ against z/h are shown in Figure 27. Note that less variation of stress intensity with distance from the center plane of the plate is predicted for both plate thicknesses, and further, that the results do not change significantly from one plate thickness to the next. The average interior value for the

stress intensity factor is also influenced by the change in grid pattern.

Figure 28 shows the influence of the surface constraint on the variation of the stress intensity factor across the plate thickness. Note that this influence is only local, i.e., near the plate surface. The extent of the observed difference between the results for the stress intensity factor constrained and free at the plate surface is influenced by grid pattern. As the thickness of grid layers near the surface is decreased, the constraint is found to have a more local effect.

These results give the reader a measure of the inaccuracies in predictions which can result even with the use of singularity elements. The explanation for these discrepancies is related to the use of the singularity solution to model the solution throughout the singular elements. The asymptotic solution, equation (14), is applicable in regions close to the crack edge, i.e., distances r which are small compared to the other geometric dimensions. For the first grid pattern, the core element radius is not sufficiently small in comparison with the plate thickness, and, as a result, the plane strain condition assumed for the singular solution is violated over a significant portion of these elements.

These results demonstrate that the region over which the plane strain singularity holds is directly related to plate

thickness. Thus, if a crack growth criterion is applied at some absolute distance r_0 from the crack edge, increased variation of growth along the crack front will be predicted as plate thickness is decreased. This prediction is consistent with experimental observations.

C. Crack Growth Modeling

Calculations have been performed for various crack front shapes in conjunction with crack growth modeling. The results indicate that the variation of the stress intensity factor along the crack edge is sensitive to the details of the crack front geometry. This suggests that there may be a "natural" crack front shape, which will necessarily depend on material properties, specimen geometry, and loading, at which unstable fracture can occur. The concept is supported by experimental observations [7] for specimens of only moderate thickness. When a fatigue crack is grown from an initial straight cut, the crack front quickly develops a curved shape which is then maintained during further fatigue crack propagation. The shape of the crack front is influenced by the amplitude of the loading cycles with generally increased curvature accompanying increased load amplitude. If a monotonic loading is then applied, crack growth initiates stably in the specimen interior thereby increasing the front curvature. Instability and the development of shear lips (nonplanar crack front growth) are observed to occur at about the same time.

Consider the crack growth process under monotonic loading. The load-load point displacement record for a crack growth process involving a moderate thickness specimen can be characterized by a linear portion, a nonlinear regime and an instability (Figure 29). In the linear range, no significant growth or yielding is occurring. On the other hand, during the nonlinear (yet stable) portion of the curve, both plastic deformation and stable growth may be occurring simultaneously. The relative contributions of these two phenomenon will depend on material properties, geometry (thickness), and load. The crack growth components clearly dominates at instability.

It appears necessary to be able to characterize the separate contributions of plastic deformation and stable crack growth and to understand how they vary with geometry and material properties, in order to be able to predict the crack growth process in a structural component based on specimen test data.

The goals of this research effort are to model the stable growth process described above by separately analyzing the influences of crack front geometry (local growth) and the contributions from material nonlinearity. The subsequent aim is to account for these two contributing factors simultaneously and thereby predict the crack growth process under monotonic loading in terms of material properties and geometry.

In this section, results of three-dimensional elastic finite element analyses are used in conjunction with a local growth criterion to predict increments of crack growth and corresponding changes in crack front shape. (Current efforts including plastic influences will be presented in a later report). The approach employed here yields meaningful information concerning crack front shape and changes in specimen compliance; however, it is incapable of treating the question of stability because it does not account for material irreversibility.

D. Local Crack Growth Criterion

In general, both the direction and magnitude of local crack growth from the current crack front are expected to vary with position along that front. The strain energy density field surrounding the crack front is the basis for the development of the local crack growth criterion to be considered here [8-10]. It is postulated that the path of growth from each point along the crack edge will follow the minimum strain energy density path emanating from that point. Further, growth at points along the current crack front will initiate when the strain energy density at a "core" distance (r_0) along the minimum path reaches a preset value W^*.

Hence, the continuous growth of the crack front is approximated by discrete increments of growth. The amount of growth at a point along the crack front in an increment is taken to

be the distance along the minimum strain energy density path to the point where the strain energy density reaches a preset value, W^*, (dependent on the material characteristics). A graph containing plots of strain energy density, W, against distance along the minimum path (r) normal to the crack edge from the associated points on the crack front is employed to predict the new crack front geometry, e.g., Figure 30. It should be observed that the value chosen for W^* will influence the magnitude of growth and the shape of the subsequent crack fronts. The results from an example set of calculations are shown in Figures 31-34. Figures 31-33 show the strain energy density curves and Figure 34 displays the predicted crack front geometry with each increment in growth. In this case, all increments of growth are predicted at the same load level. The changes in specimen compliance with crack growth are given in Table 2.

TABLE 2 - CHANGES IN COMPLIANCE WITH CRACK GROWTH

Increment Number	Maximum Growth Along Front $\Delta a/a$	Effective Displacement of Loaded Surface $\tilde{U}E/\sigma_0 c$
1	0	2.700
2	0.02	2.756
3	0.04	2.810
4	0.06	-

Note, a current limitation of the finite element crack tip element formulation discussed earlier is that the crack front must be normal to the plate surface at the point of intersection. (Other three-dimensional crack tip elements such as the quarter point elements [11] and Tracey's pie shaped elements [12] are also subject to this limitation). Minor adjustments of the predicted shape of crack growth increments are imposed to satisfy this restriction.

Some additional information of potential interest obtained from the finite element results includes:

(a) The variations of the stress intensity factor along the crack front at each increment - see Figure 35. The rapid variations predicted in the vicinity of the free surface are believed to be a result of forcing a 90° intersection between the crack front and the specimen surface.

(b) The variations of the distortional strain energy density component directly ahead of the existing crack front (at $\theta = 0°$) shown in Figure 36.

The fact that the distortional component of strain energy density, normally associated with plastic deformation, increases as the free surface* is approached and does so more rapidly

*The decrease in distortional strain energy density, in the immediate vicinity of the surface may be the result of numerical inaccuracies.

for curved crack fronts than straight ones implies the development of plastic constraint at the surface and the formation of shear lips.

REFERENCES

[1] Plane Strain Crack Toughness Testing of High Strength Metallic Materials, edited by W. F. Brown, Jr., and J. E. Srawley, ASTM Special Technical Publication No. 410, (1966).

[2] Hilton, P. D., Gifford, L. Nash, Jr., and Lomacky, O., "Finite Element Fracture Mechanics Analysis of Two-Dimensional and Axisymmetric Elastic and Elastic-Plastic Cracked Structures", NSRDC Report 4493, (November 1974).

[3] Gifford, L. Nash, Jr., "Apes-Second Generation Two-Dimensional Fracture Mechanics and Stress Analysis by Finite Elements", NSRDC Report 4799, (December 1975).

[4] Hutchinson, J. W., "Plastic Stress and Strain Fields at a Crack Tip", J. Mech. Physics and Solids, Vol. 16, (1968).

[5] Sih, G. C., Hilton, P. D., Hartranft, R. J. and Kiefer, B. V., "Three-Dimensional Stress Analysis of a Finite Slab Containing a Transverse Central Crack", Technical Report IFSM-75-69, Lehigh University, (June 1975).

[6] Zienkiewicz, O. C., The Finite Element Method in Engineering Science, McGraw-Hill, London, (1971).

[7] Miller, G. A. and Stephenson, E. T., "The Effect of the Carbide Phases on the Crack Growth of 0.5% Mo-B Steels Under Impact, Cyclic, and Monotonically Increasing Loading", Metallurgical Transactions, Vol. V, pp. 659-666, (March 1974).

[8] Sih, G. C., "Application of the Strain-Energy-Density Theory to Fundamental Fracture Problems", Technical Report IFSM-73-49, Lehigh University, (1973).

[9] Sih, G. C. and Cha, B. C. K., "A Fracture Criterion for Three-Dimensional Crack Problems", Eng. Fracture Mech., Vol. 6, (1974).

[10] Sih, G. C., ed., "A Special Theory of Crack Propagation", Methods of Analysis and Solutions of Crack Problems, Vol. 1, Noordhoff International Publishing, Leyden, The Netherlands, (1973).

[11] Barsoum, R. S., "On the Use of Isoparametric Finite Elements in Linear Fracture Mechanics", International Journal for Numerical Methods in Eng., Vol. 10, pp. 25-37, (1976).

[12] Tracey, D. M., "Finite Elements for Three-Dimensional Elastic Crack Analysis", Nuclear Engineering and Design, Vol. 26, pp. 282-290, (1973).

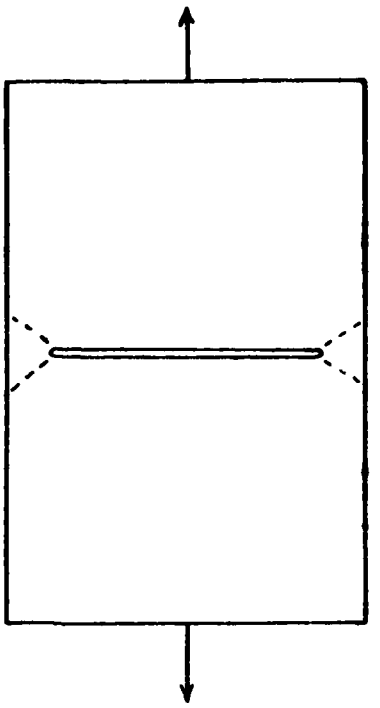

Figure 1 - Last ligament failure for a central crack specimen.

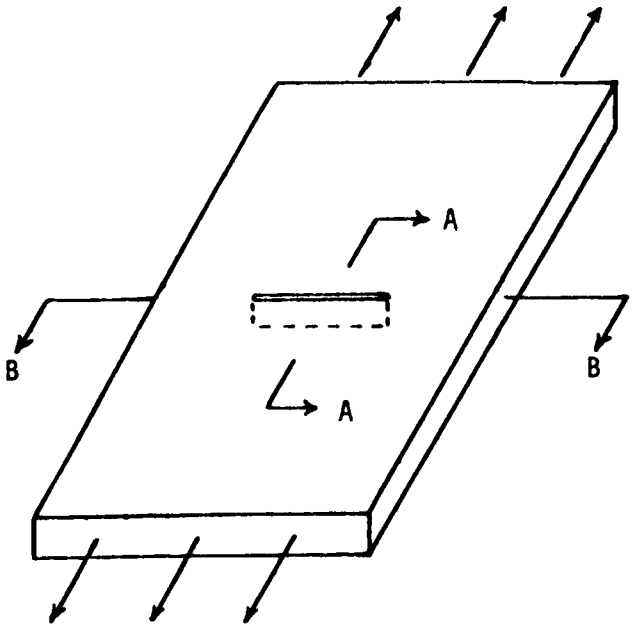

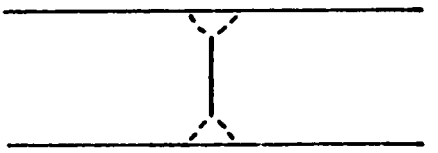

Section A-A

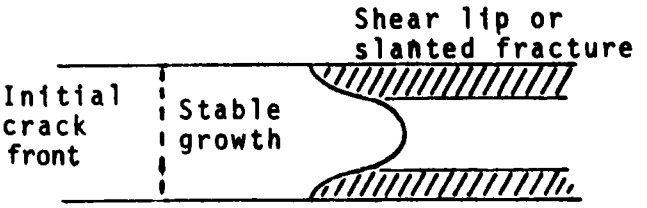

Section B-B

Figure 2 - Fracture process for center cracked specimen.

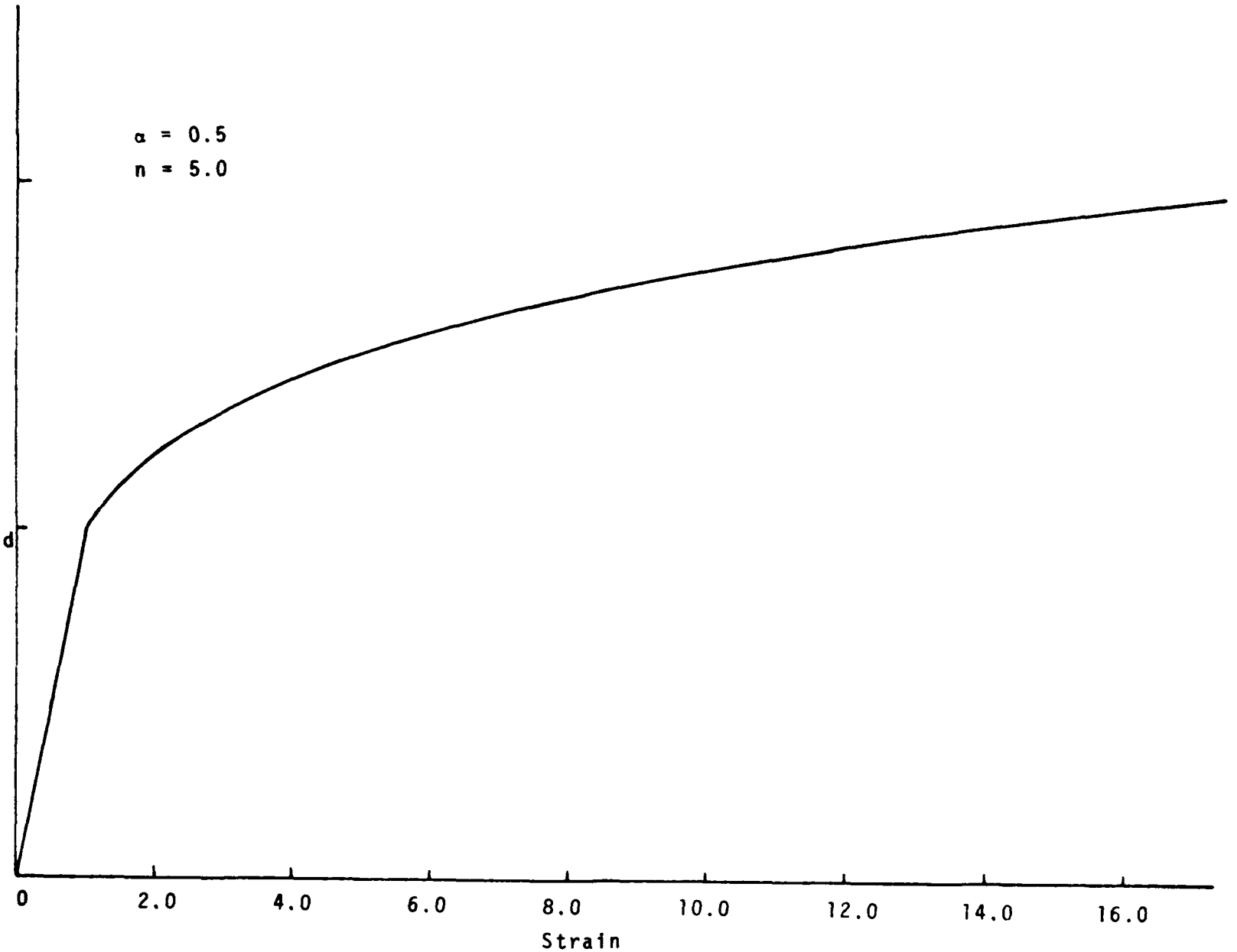

Figure 3 - Uniaxial stress strain curve.

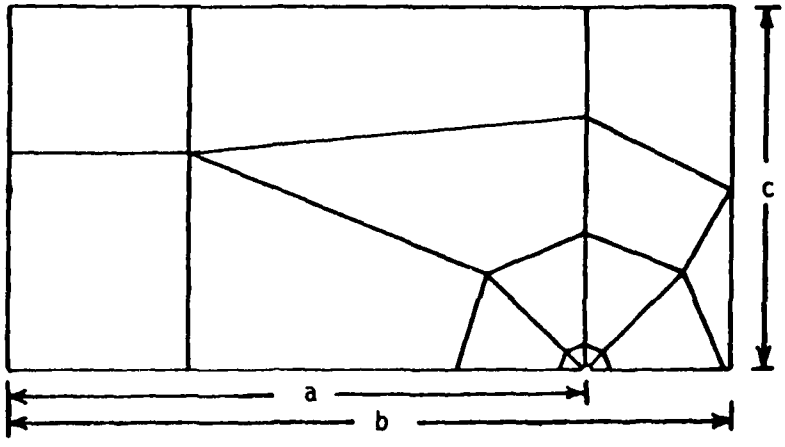

Figure 4 - Grid pattern for a 2 to 1 aspect ratio.

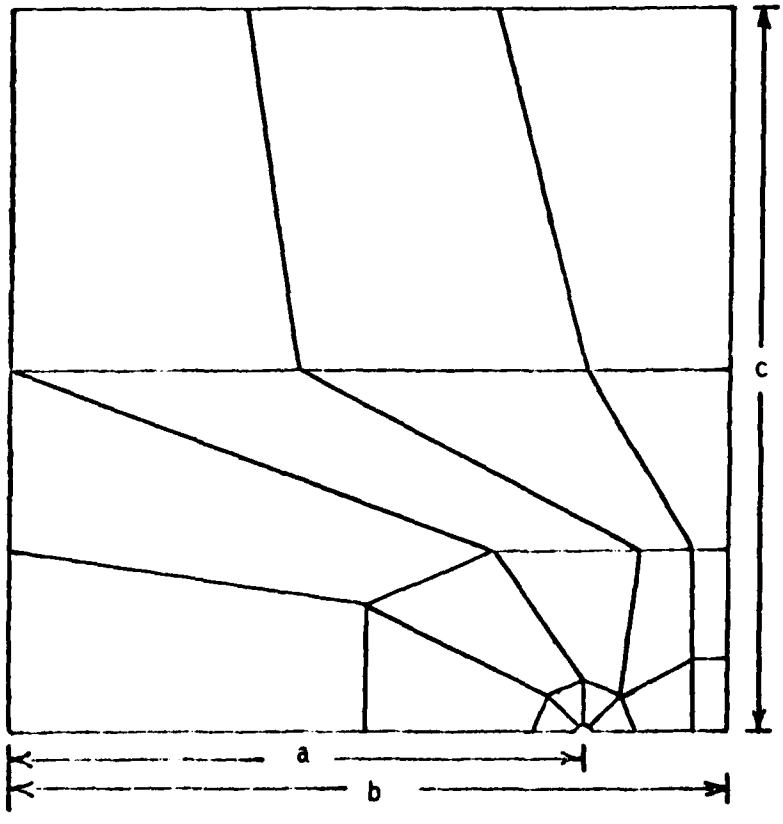

Figure 5 - Grid pattern for a 1 to 1 aspect ratio.

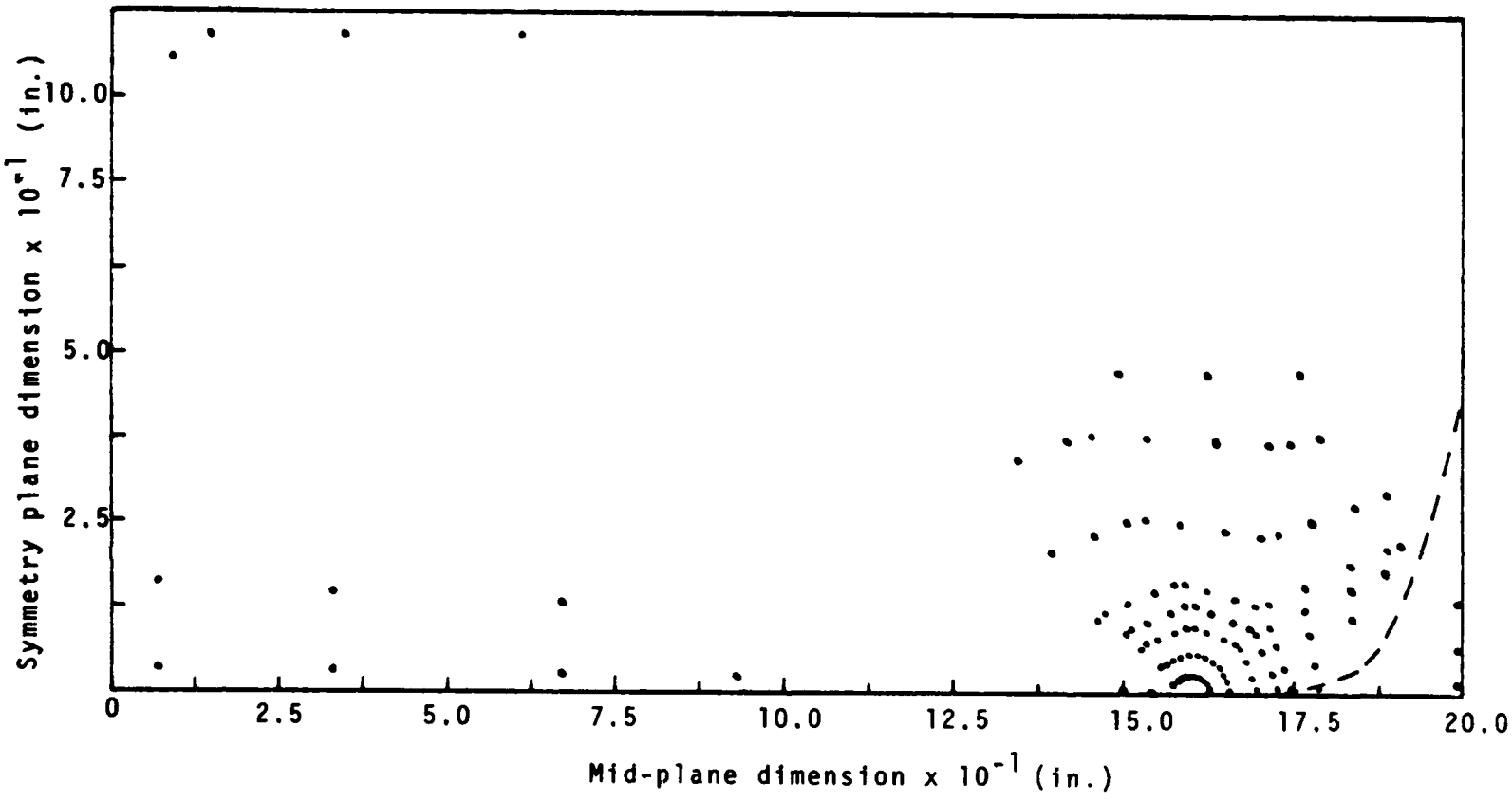

Figure 6 - Yield pattern for 2:1 aspect ratio and $\sigma = 0.28\ \sigma_{yd}$. $\frac{a}{b} = 0.8$

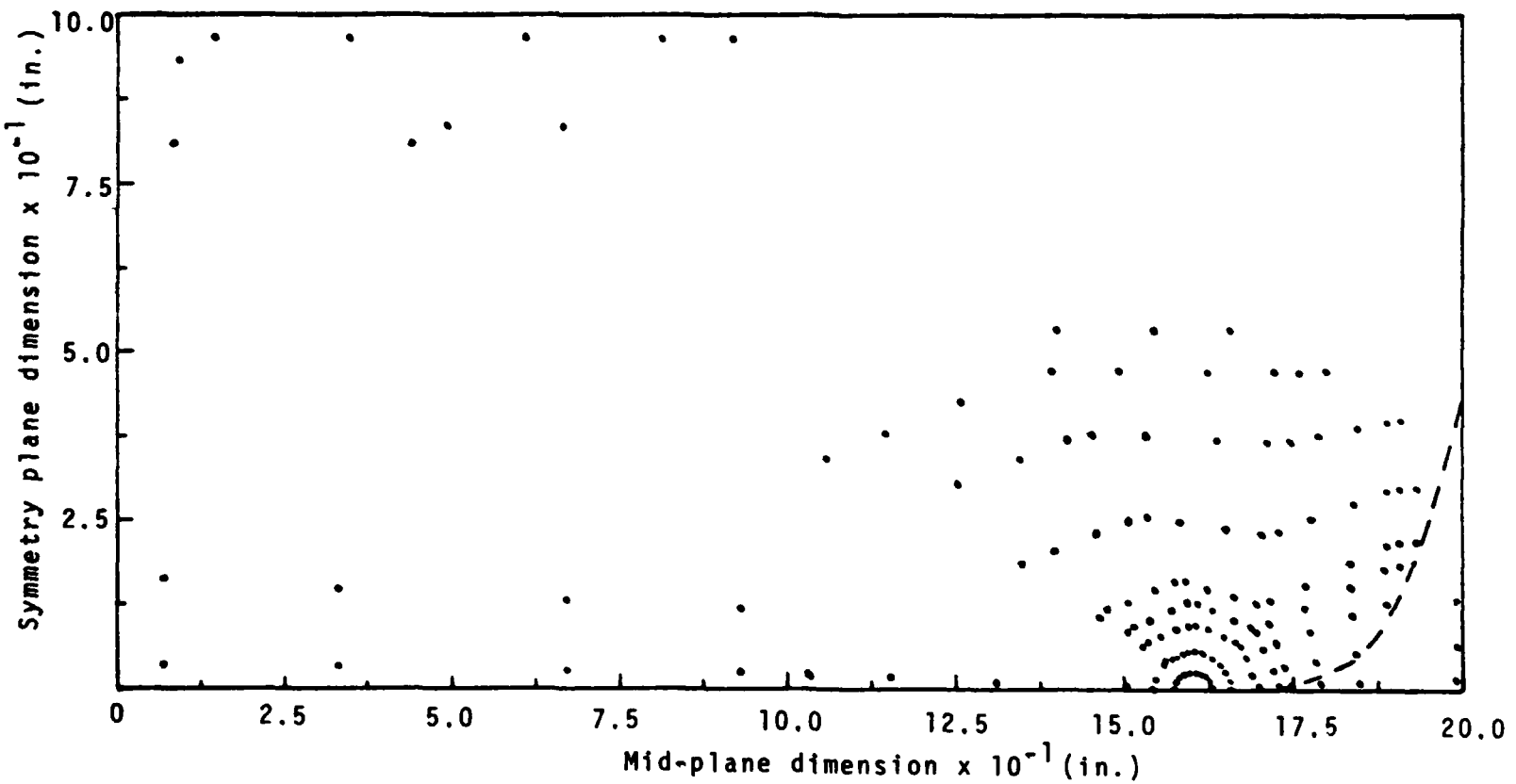

Figure 7 - Yield pattern for 2:1 aspect ratio and $\sigma = 0.31\ \sigma_{yd}$. $\frac{a}{b} = 0.8$

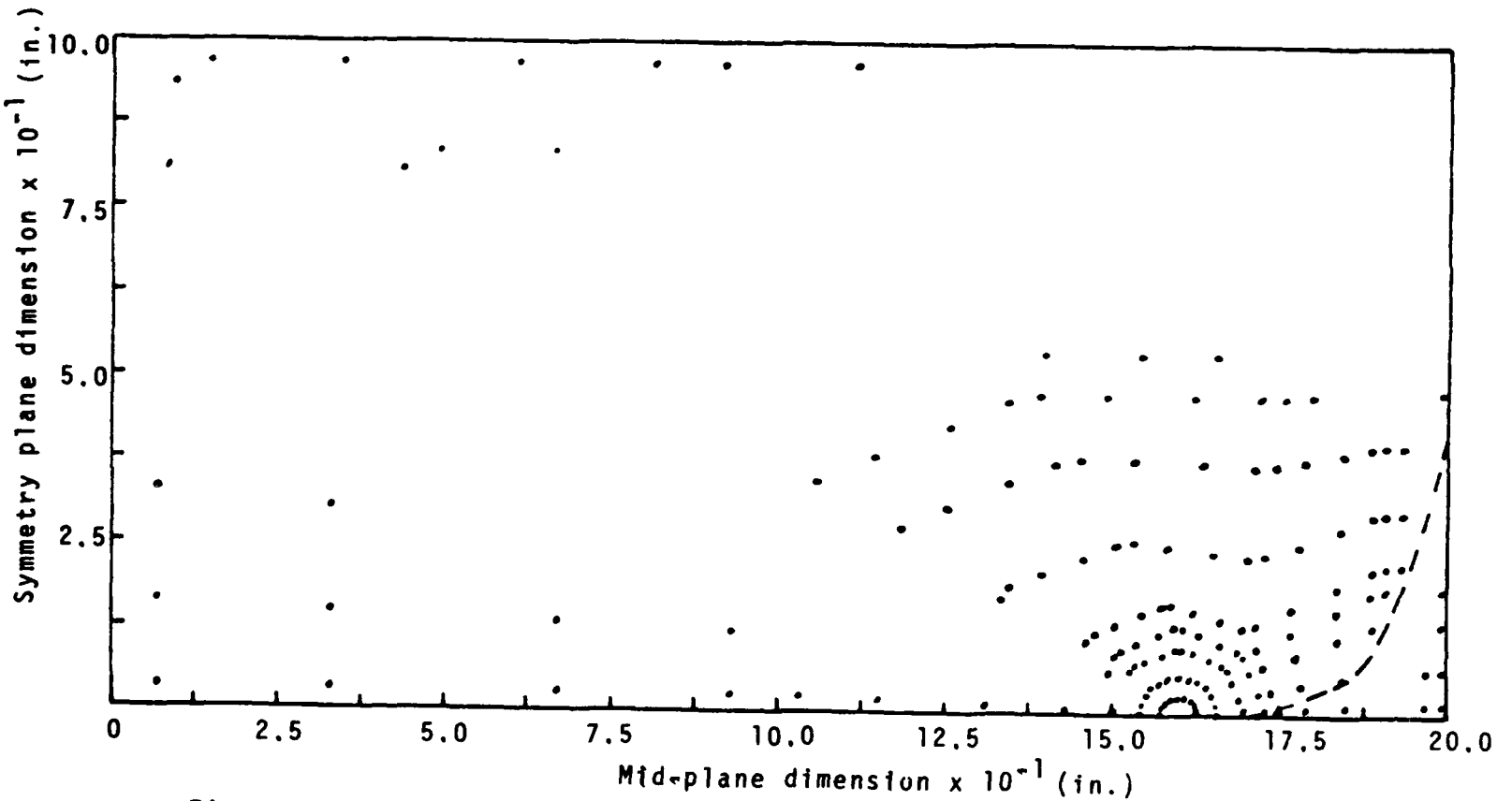

Figure 8 - Yield pattern for 2:1 aspect ratio and $\sigma = 0.35\ \sigma_{yd}$. $\frac{a}{b} = 0.8$

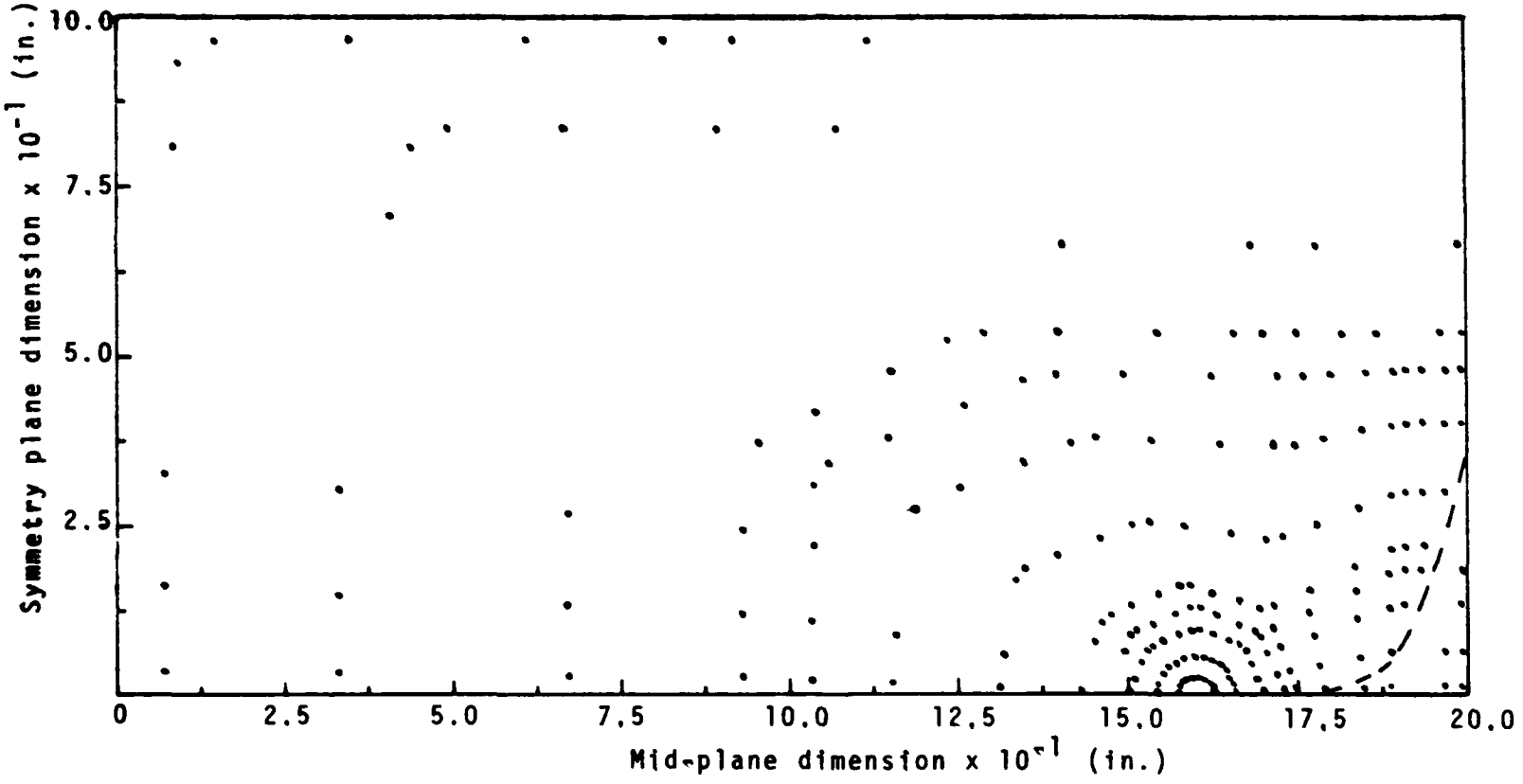

Figure 9 - Yield pattern for 2:1 aspect ratio and $\sigma = 0.38\ \sigma_{yd}$. $\frac{a}{b} = 0.8$

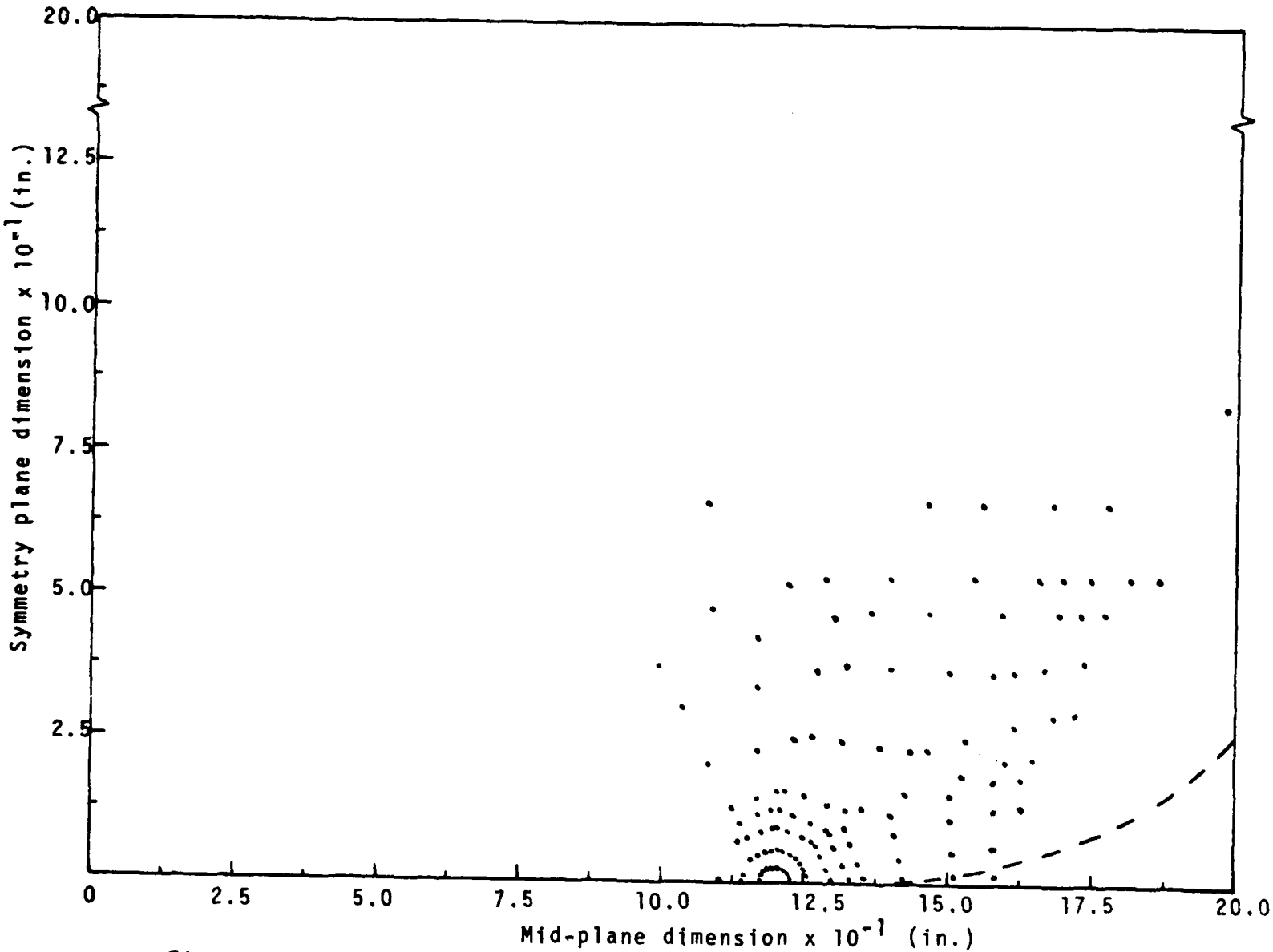

Figure 10 - Yield pattern for 1:1 aspect ratio and $\sigma = 0.28\ \sigma_{yd}$. $\frac{a}{b} = 0.6$

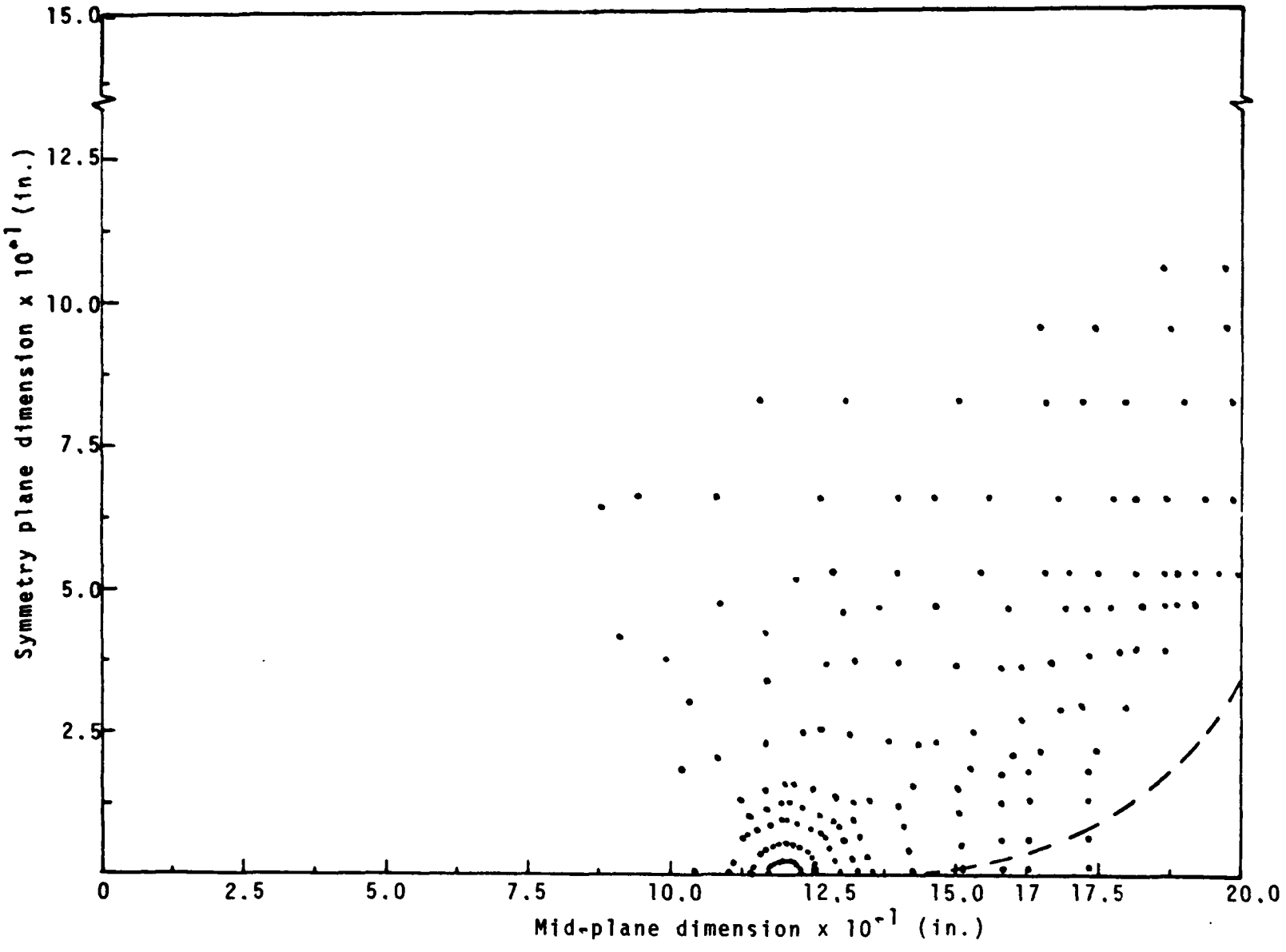

Figure 11 - Yield pattern for 1:1 aspect ratio and $\sigma = 0.31\ \sigma_{yd}$. $\frac{a}{b} = 0.6$

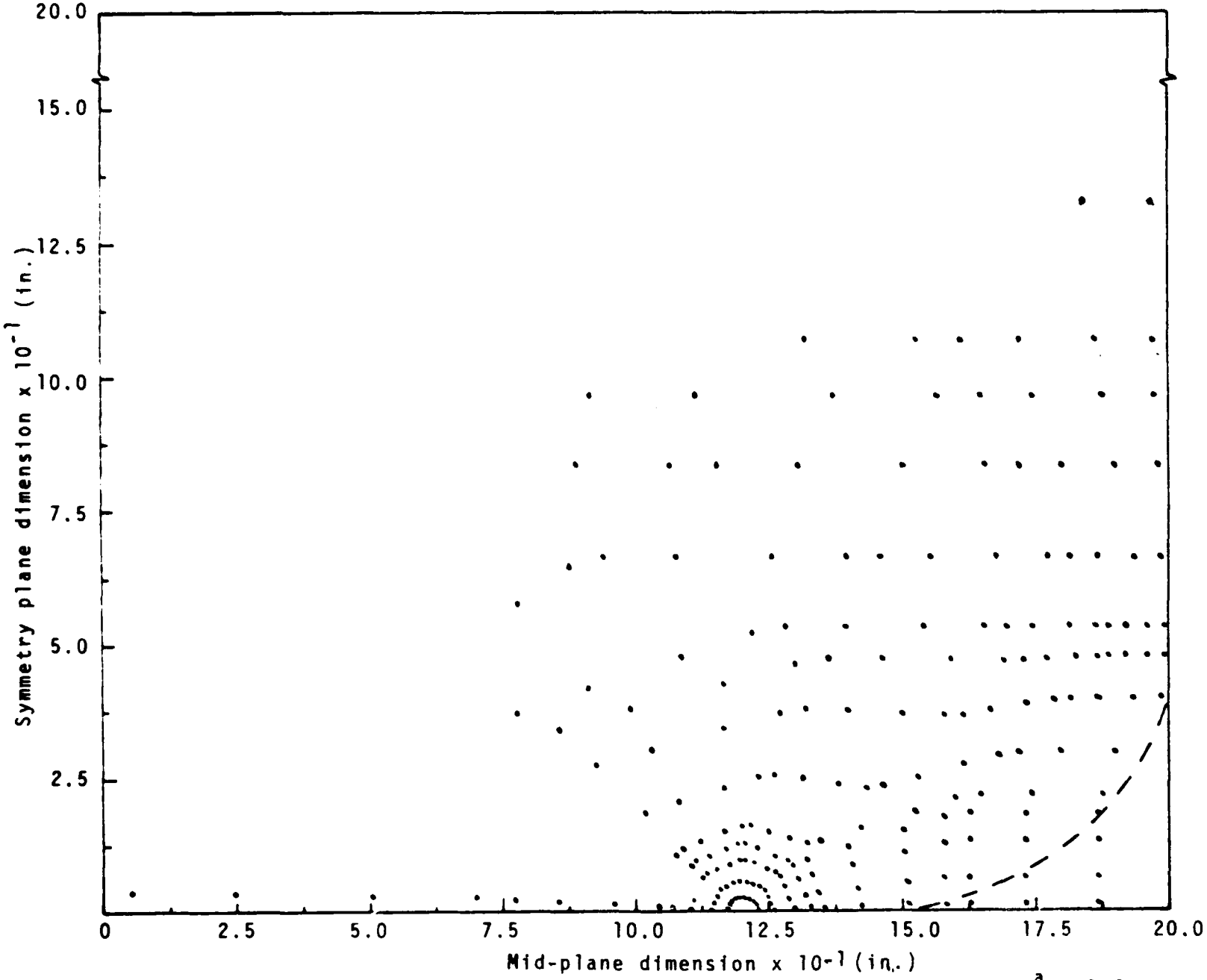

Figure 12 - Yield pattern for 1:1 aspect ratio and $\sigma = 0.36\ \sigma_{yd}$. $\frac{a}{b} = 0.6$

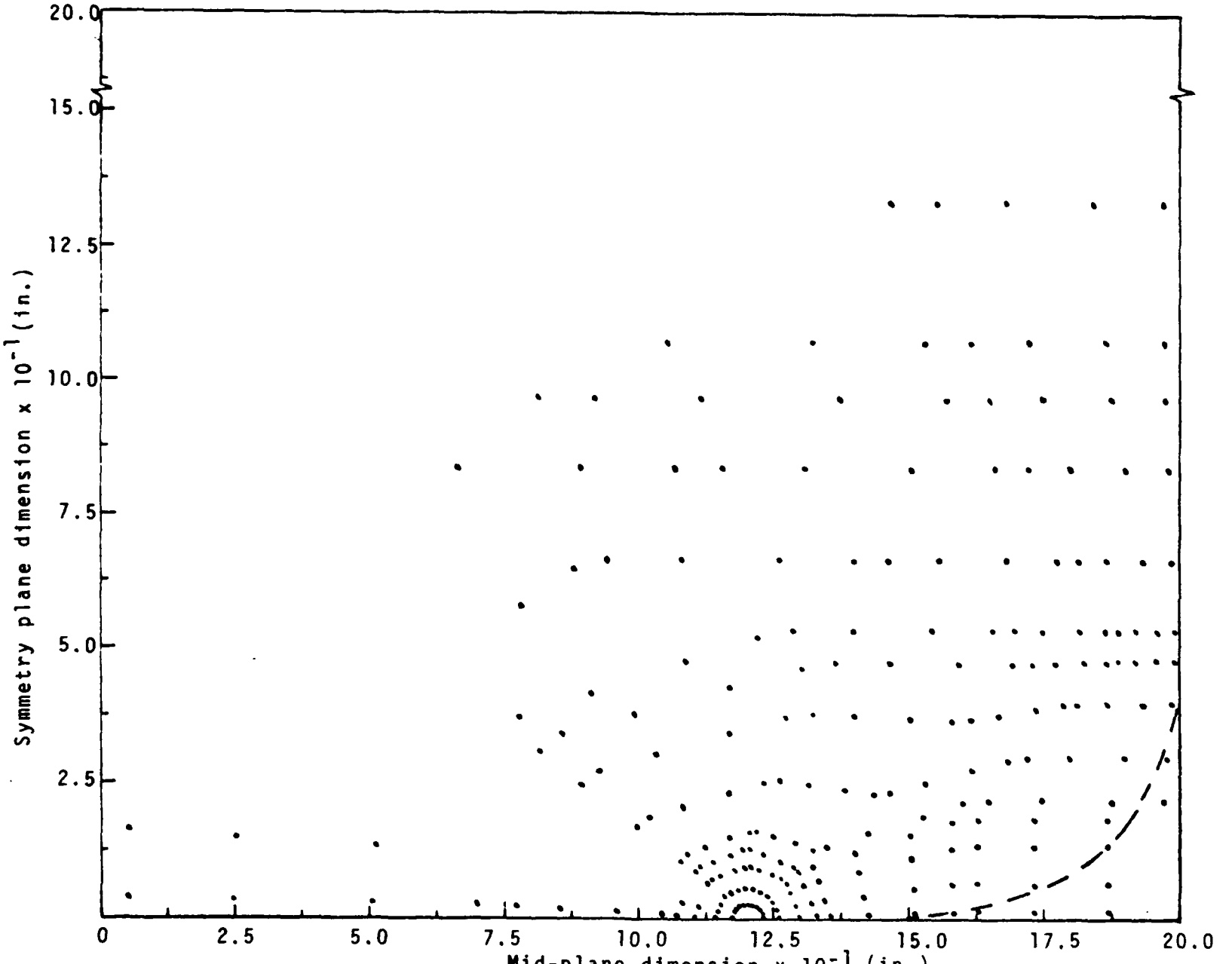

Figure 13 - Yield pattern for 1:1 aspect ratio and $\sigma = 0.38\ \sigma_{yd}$. $\frac{a}{b} = 0.6$

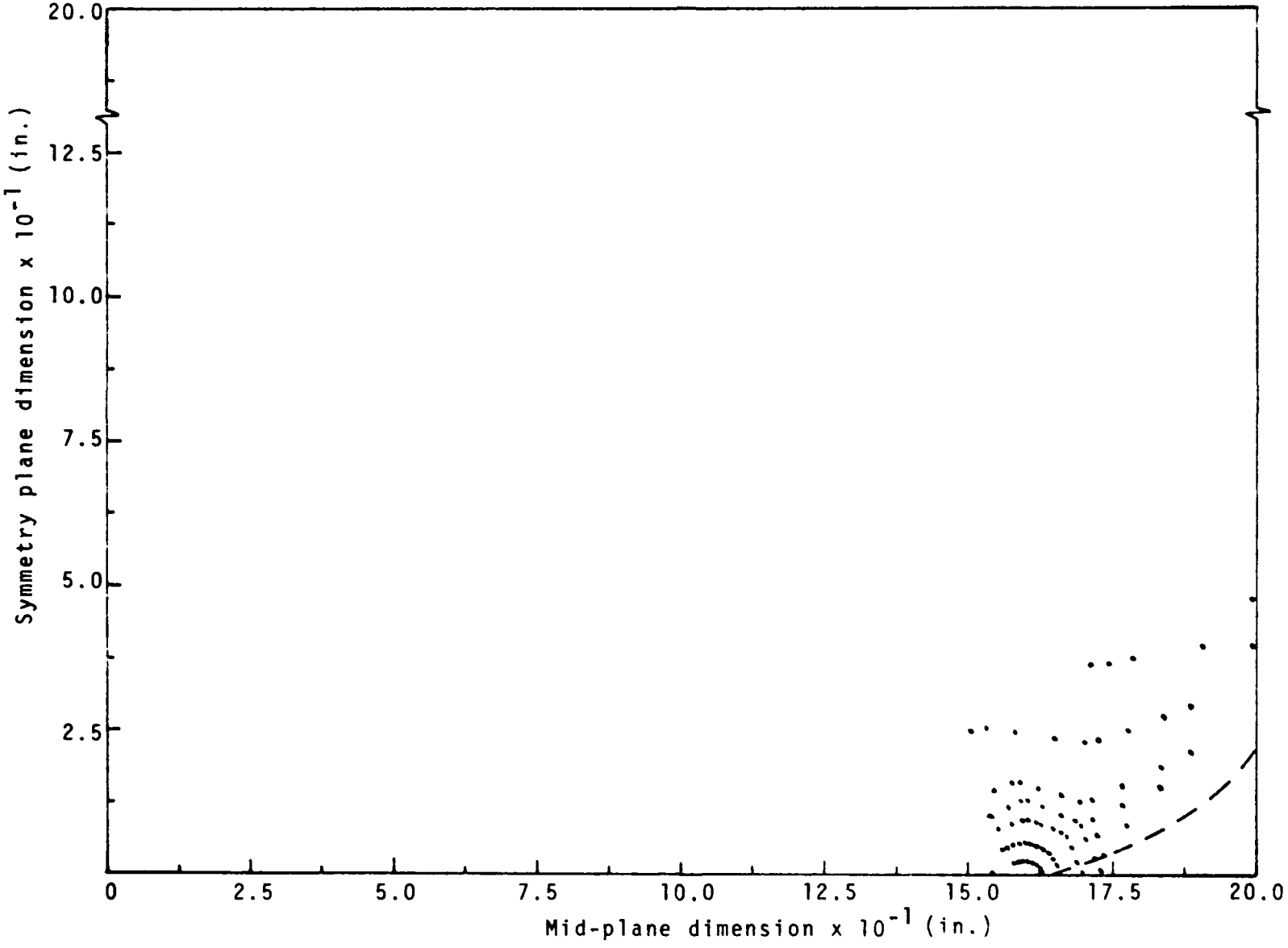

Figure 14 - Yield pattern for 1:1 aspect ratio and $\sigma = 0.28\ \sigma_{yd}$. $\frac{a}{b} = 0.8$

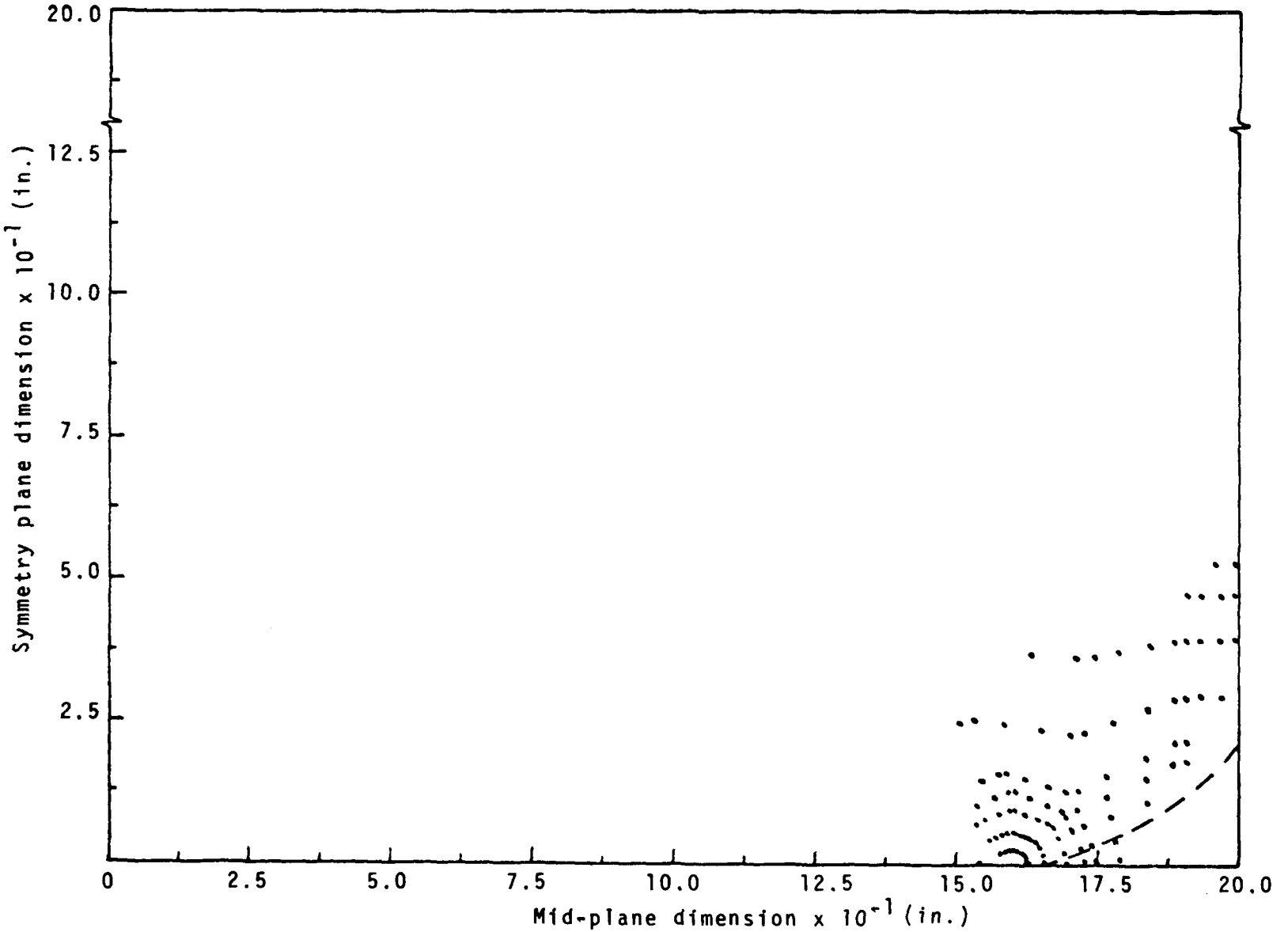

Figure 15 - Yield pattern for 1:1 aspect ratio and $\sigma = 0.30\ \sigma_{yd}$. $\frac{a}{b} = 0.8$

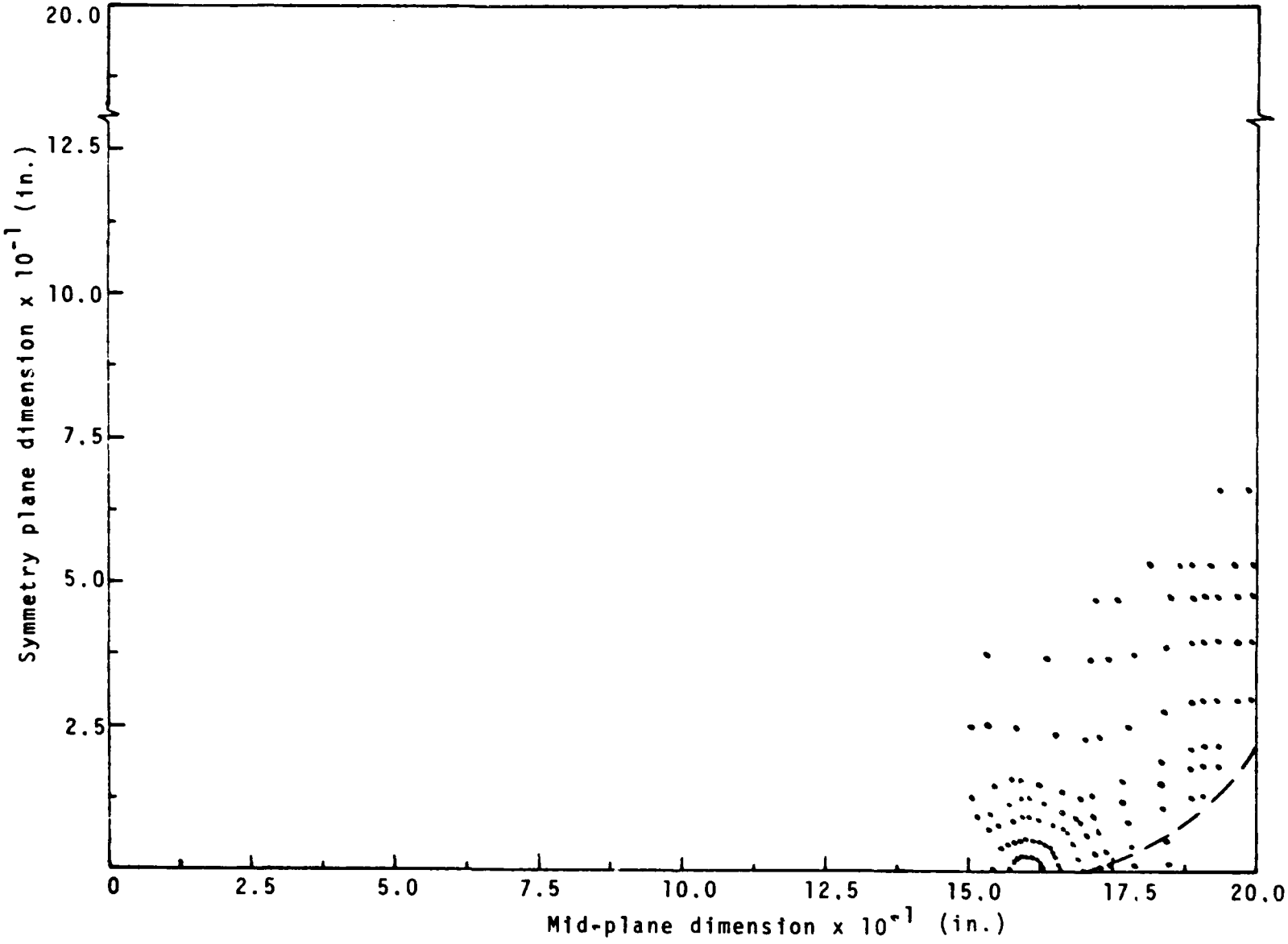

Figure 16 - Yield pattern for 1:1 aspect ratio and $\sigma = 0.32\ \sigma_{yd}$. $\frac{a}{b} = 0.8$

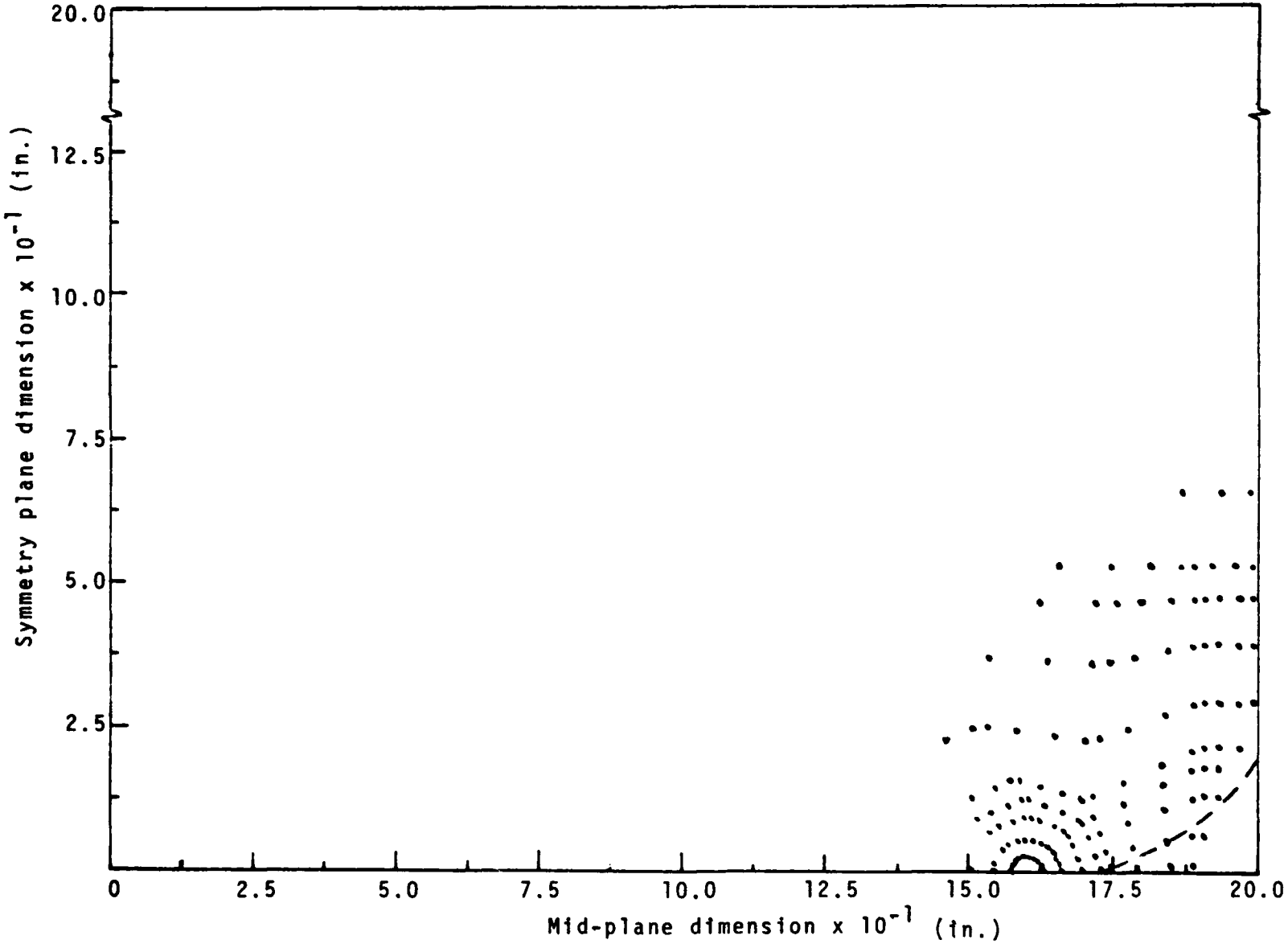

Figure 17 - Yield pattern for 1:1 aspect ratio and $\sigma = 0.34\ \sigma_{yd}$. $\frac{a}{b} = 0.8$

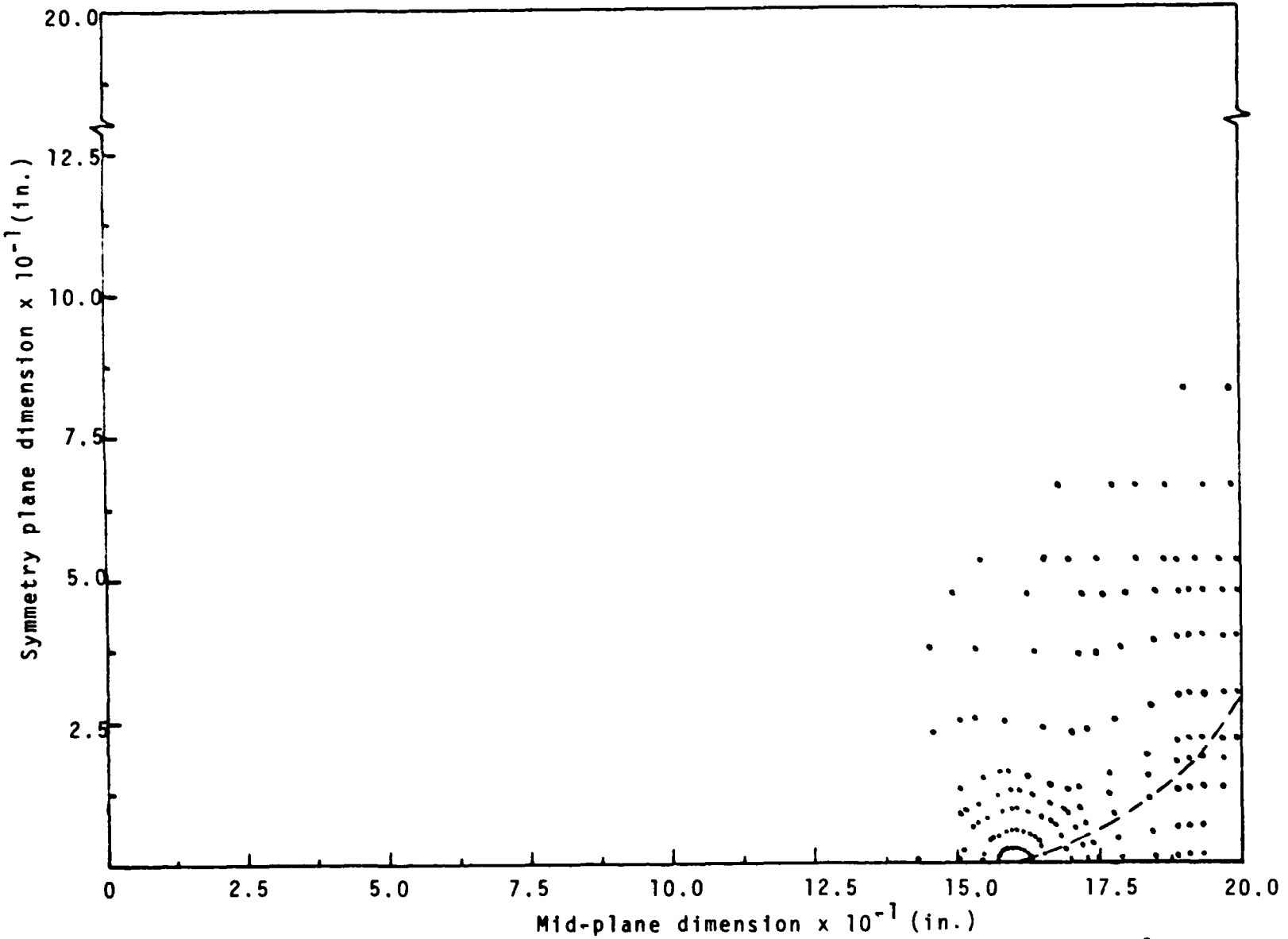

Figure 18 - Yield pattern for 1:1 aspect ratio and $\sigma = 0.38\ \sigma_{yd}$. $\frac{a}{b} = 0.8$

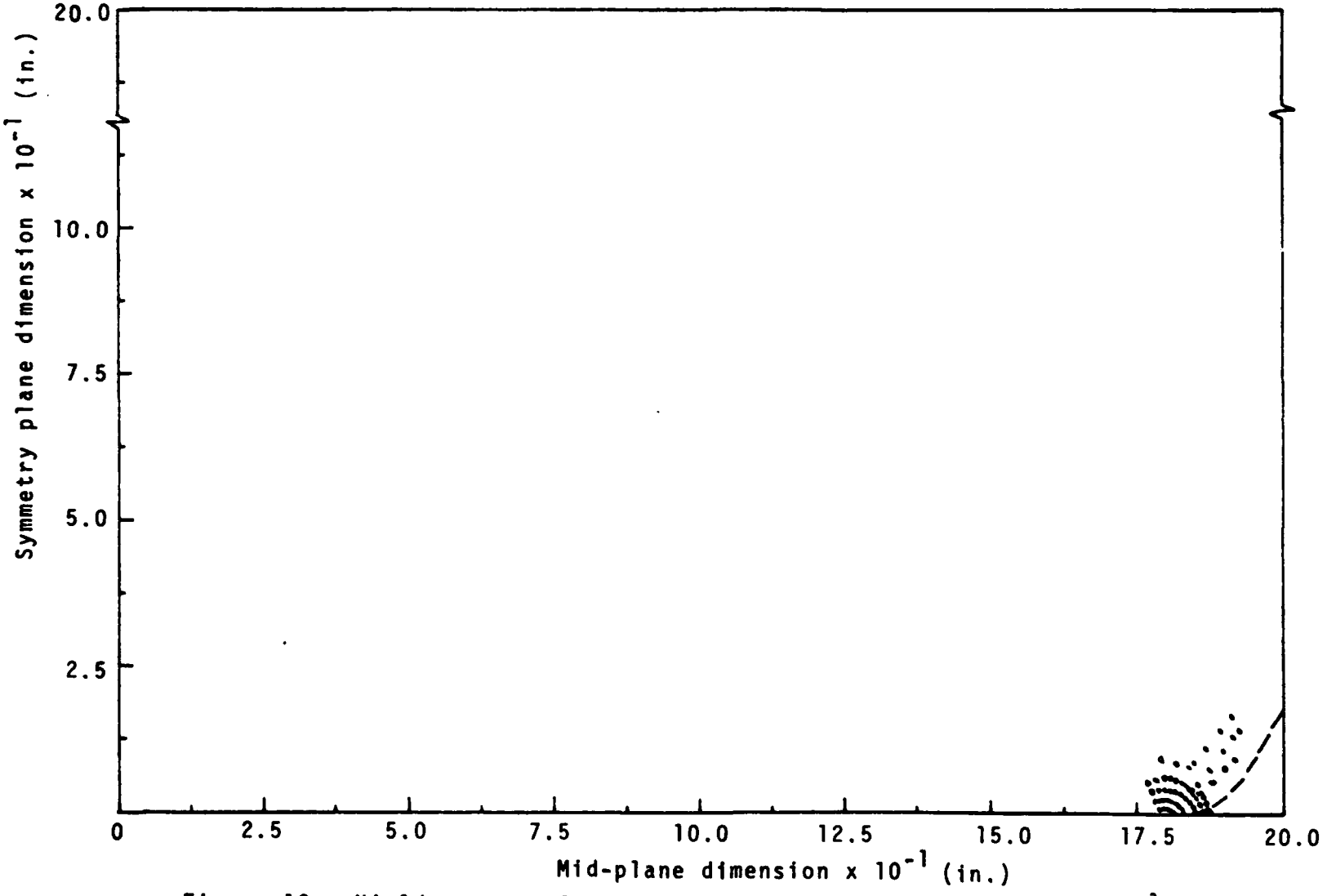

Figure 19 - Yield pattern for 1:1 aspect ratio and $\sigma = 0.28\ \sigma_{yd}$. $\frac{a}{b} = 0.9$

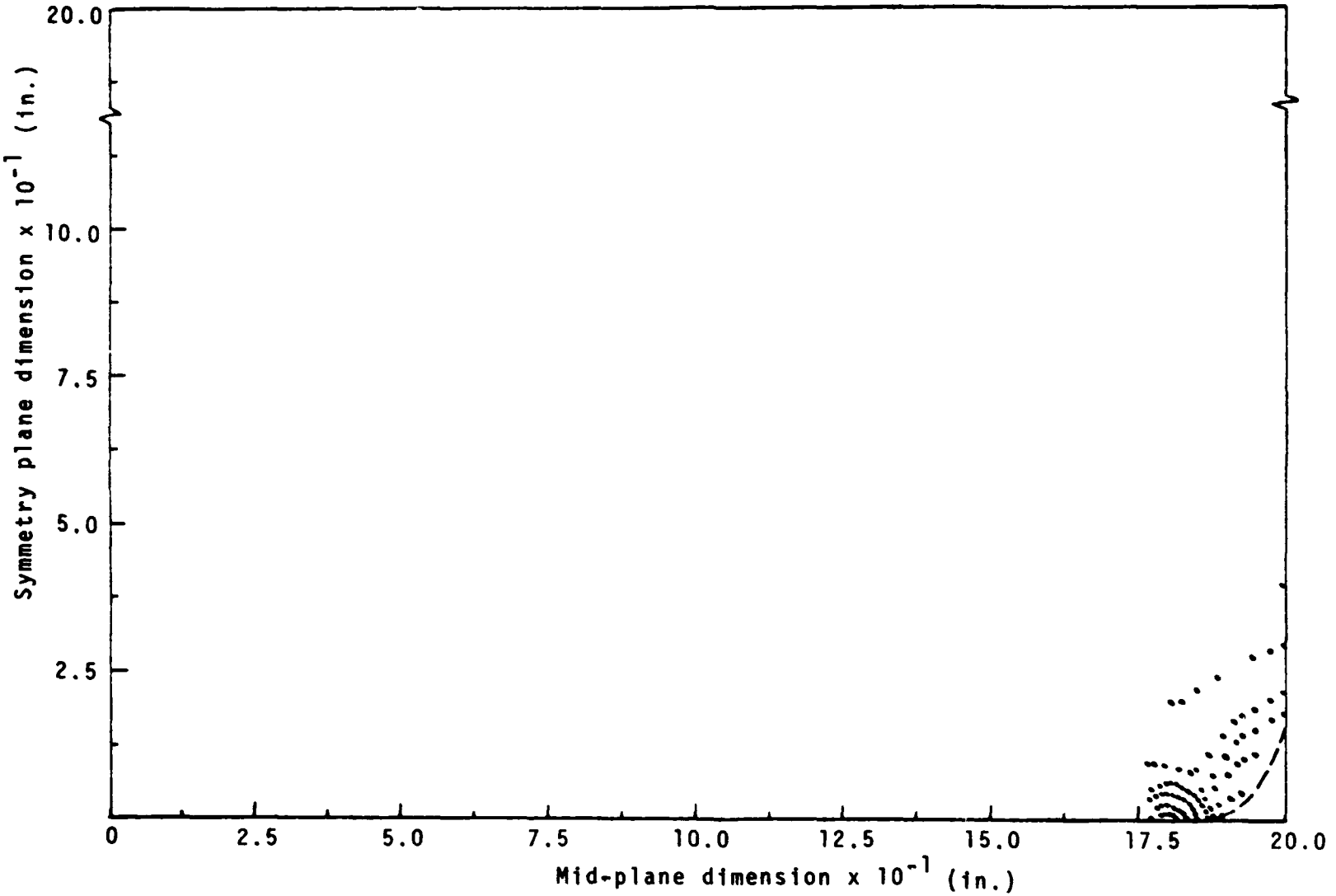

Figure 20 - Yield pattern for 1:1 aspect ratio and $\sigma = 0.31\ \sigma_{yd}$. $\frac{a}{b} = 0.9$

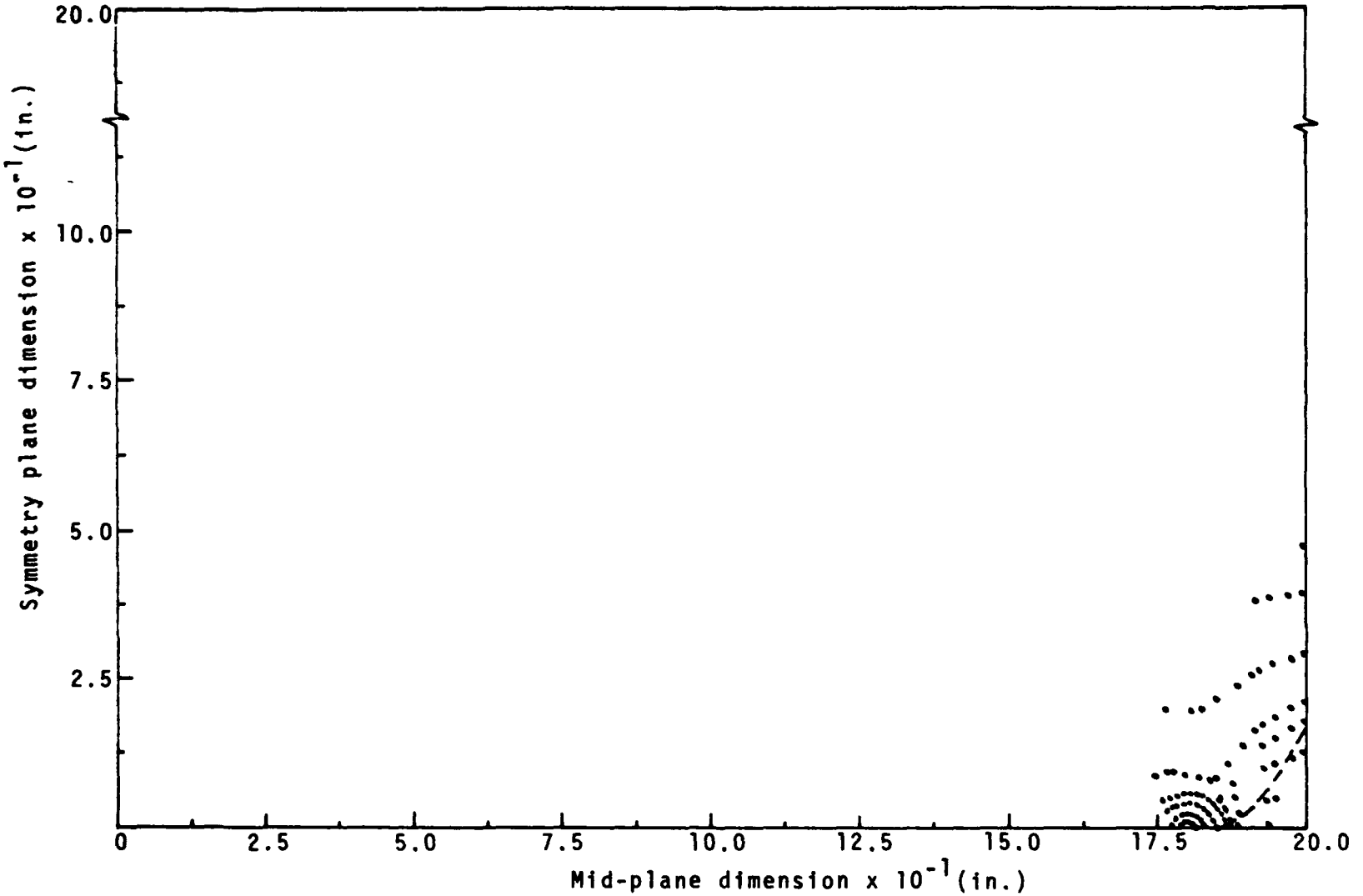

Figure 21 - Yield pattern for 1:1 aspect ratio and $\sigma = 0.36\ \sigma_{yd}$. $\frac{a}{b} = 0.9$

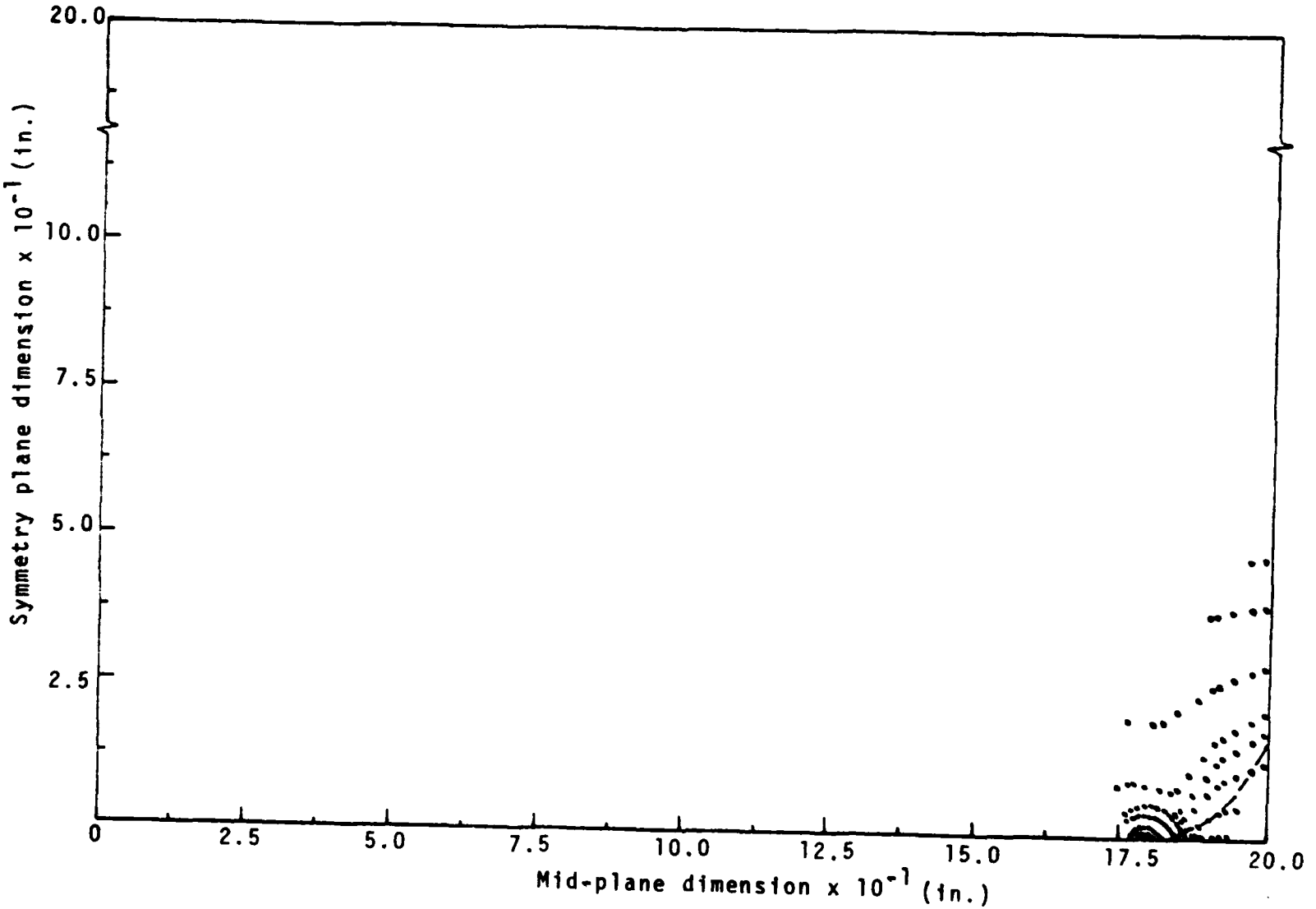

Figure 22 - Yield pattern for 1:1 aspect ratio and $\sigma = 0.38\ \sigma_{yd}$. $\frac{a}{b} = 0.9$

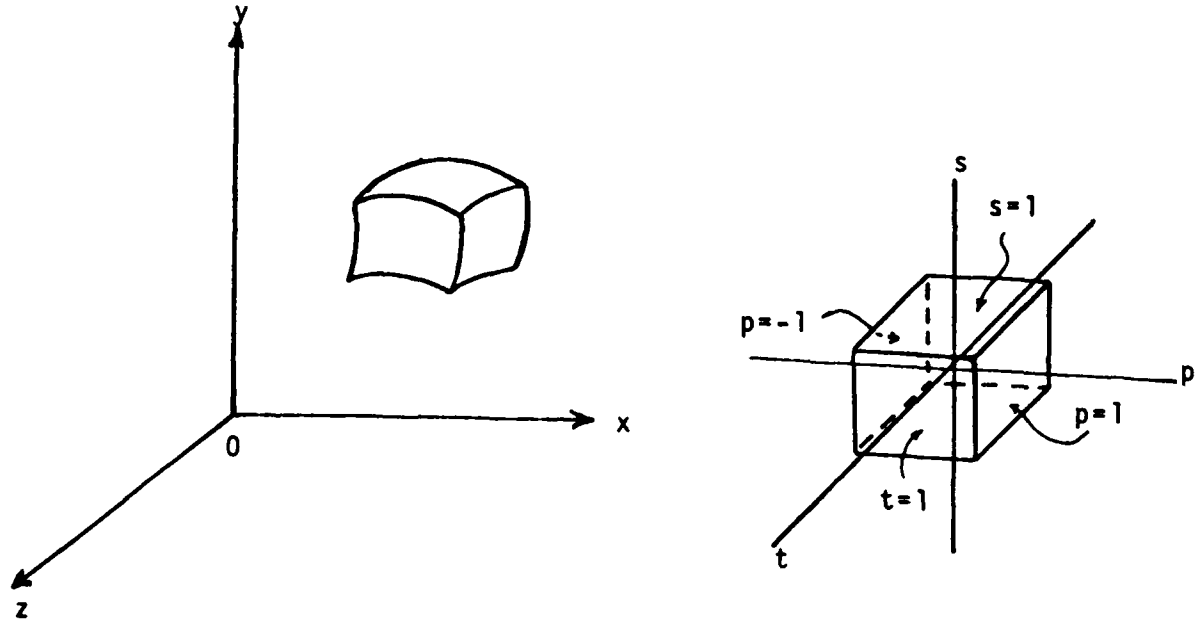

Figure 23 - Mapping of curvilinear finite elements.

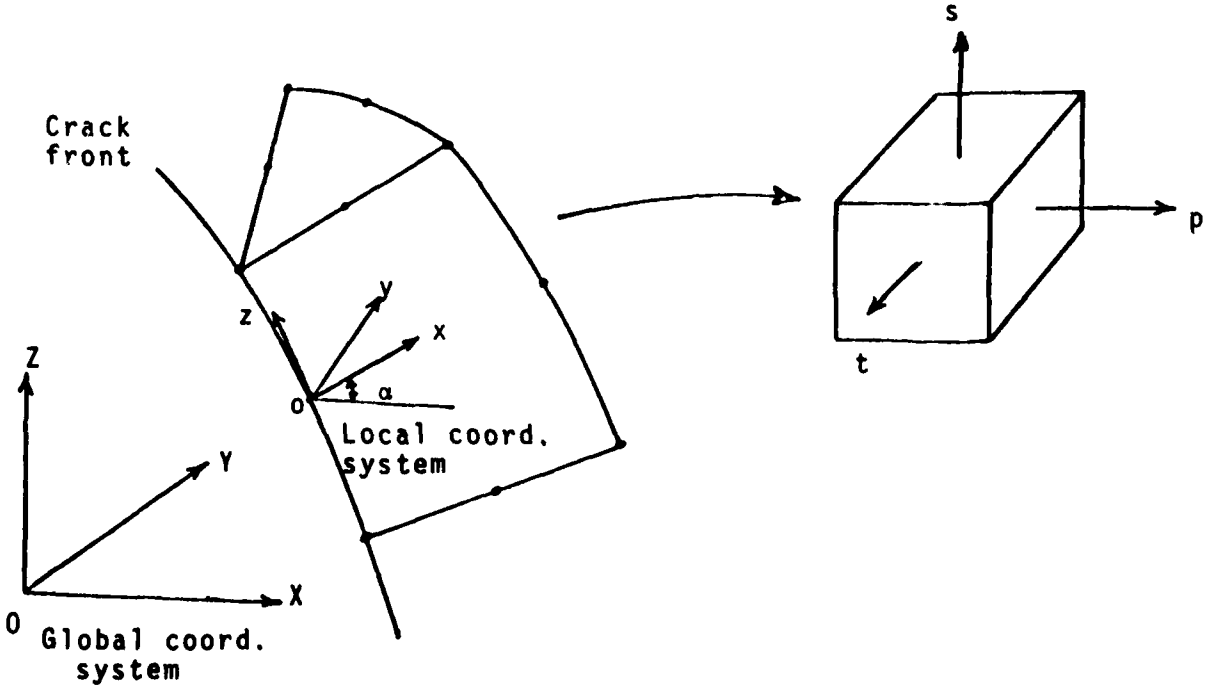

Figure 24 - Singularity element.

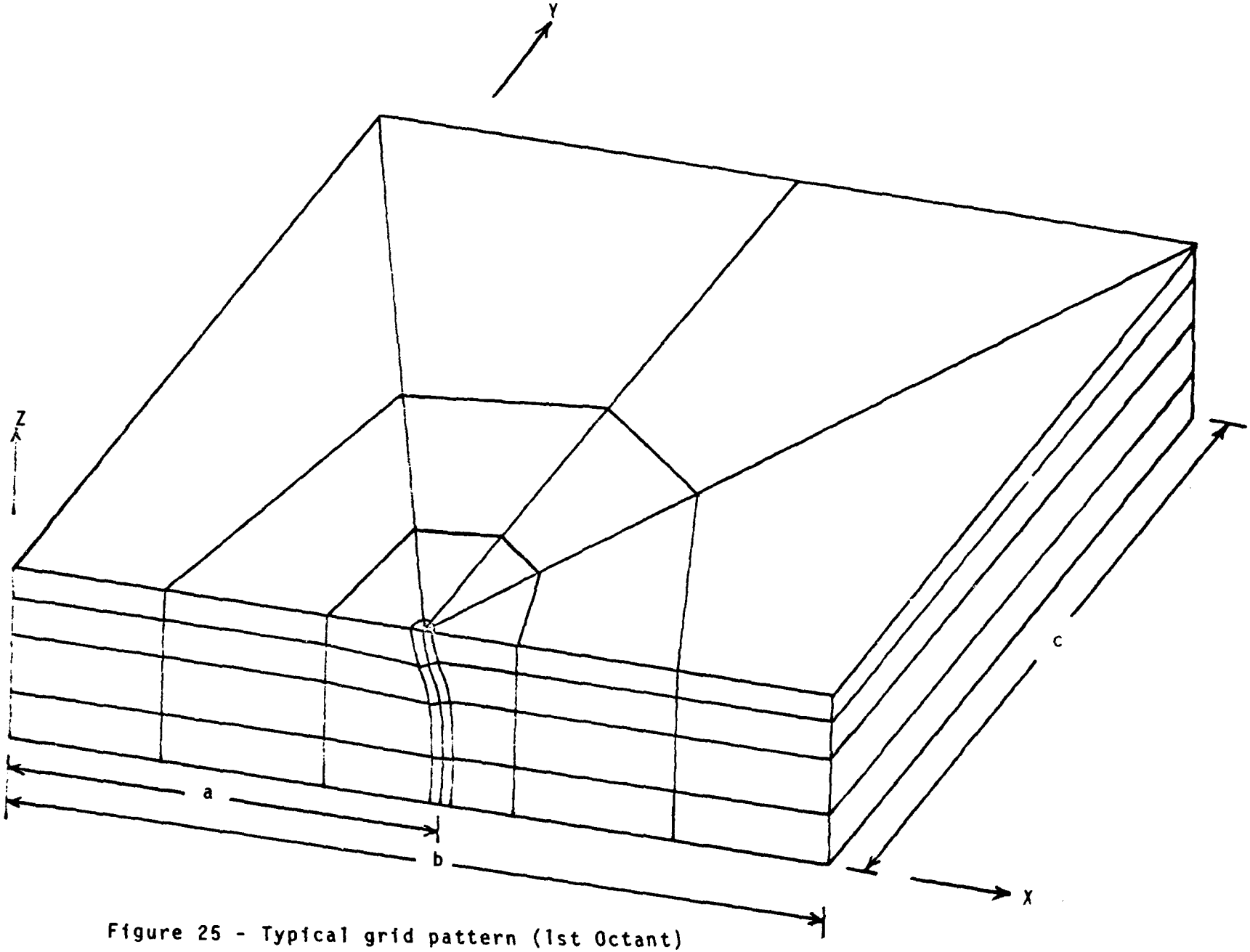

Figure 25 - Typical grid pattern (1st Octant)

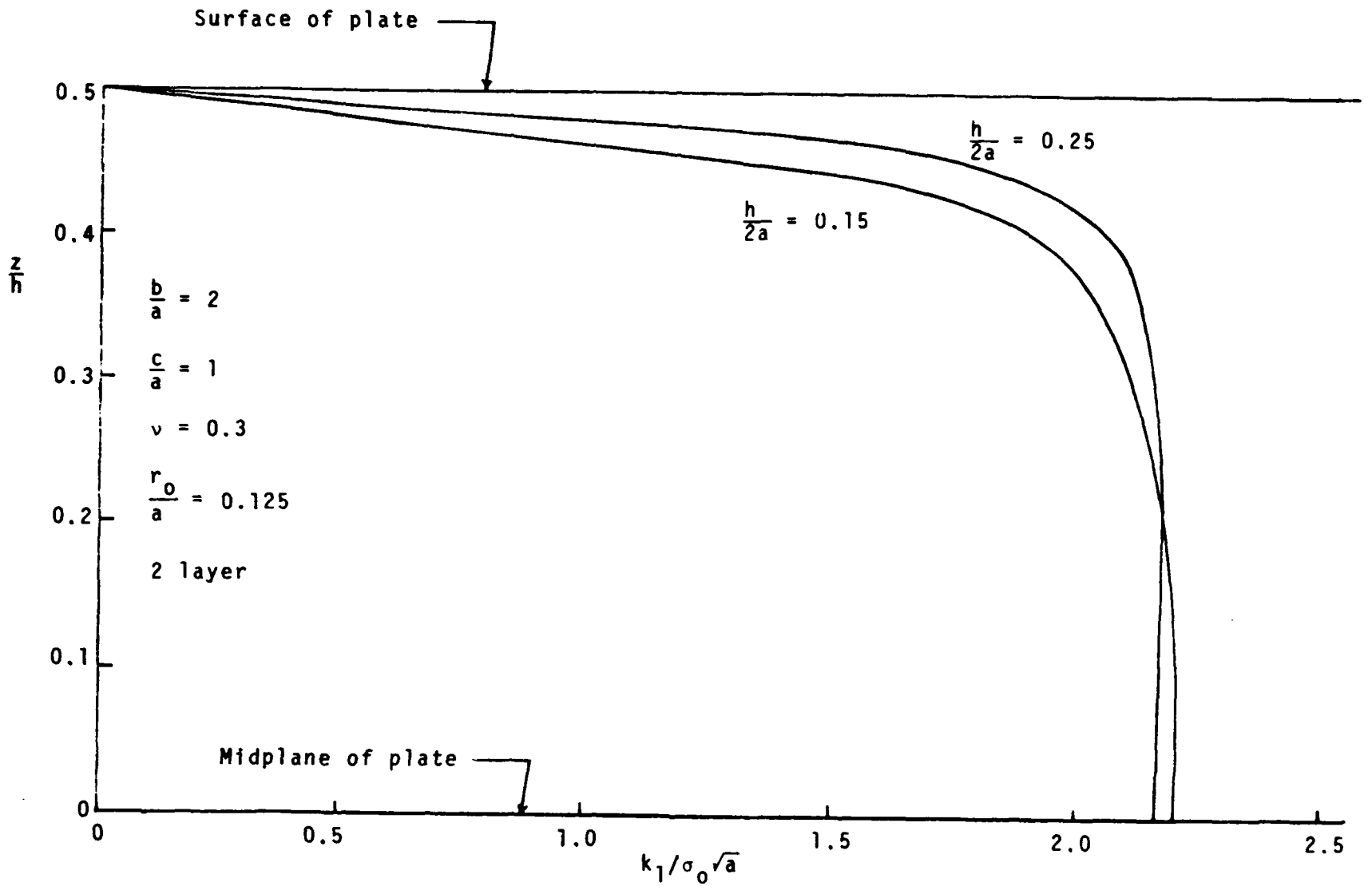

Figure 26 - Variation of stress intensity factor along crack front.

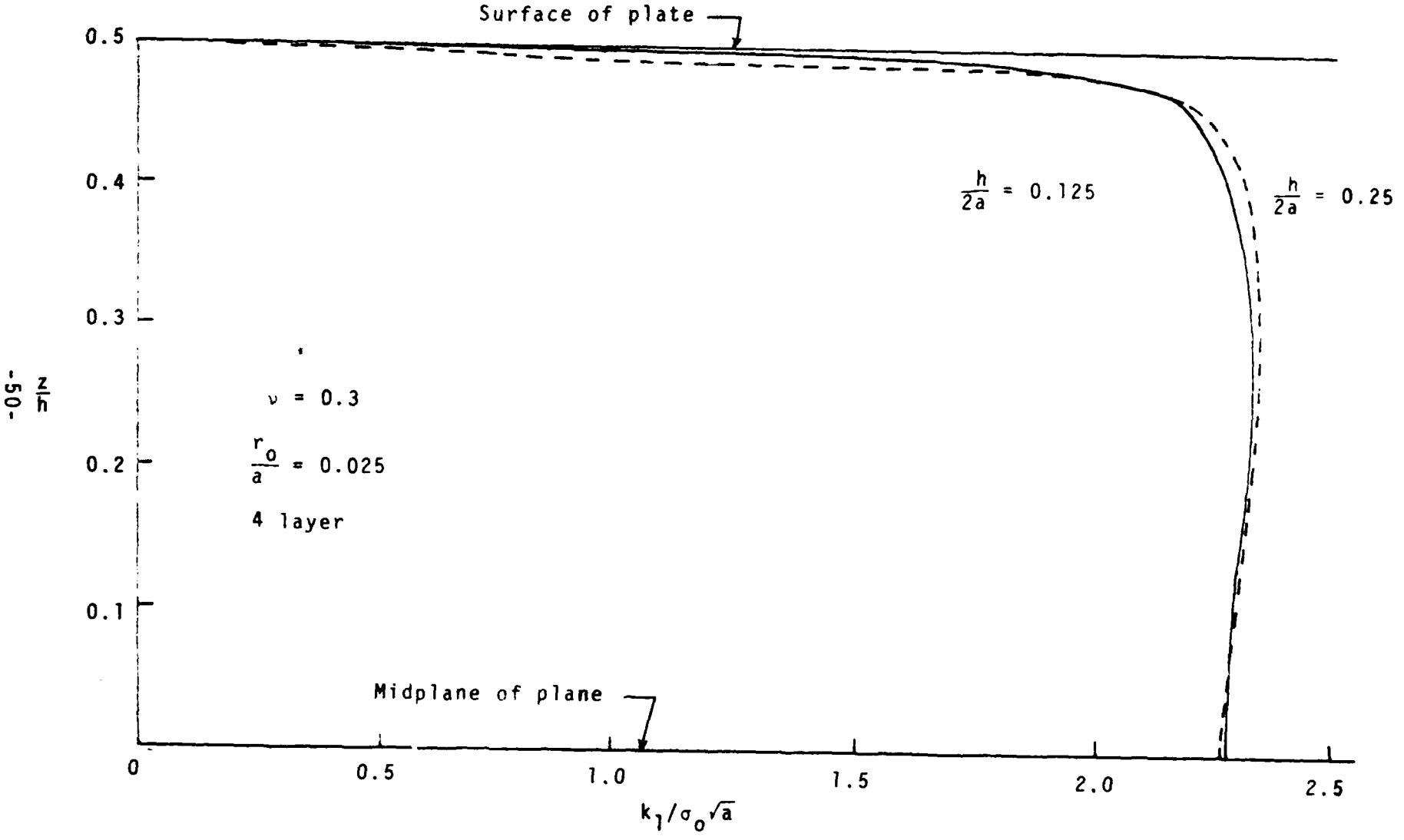

Figure 27 - Influence of element radius r_o on the stress intensity factor.

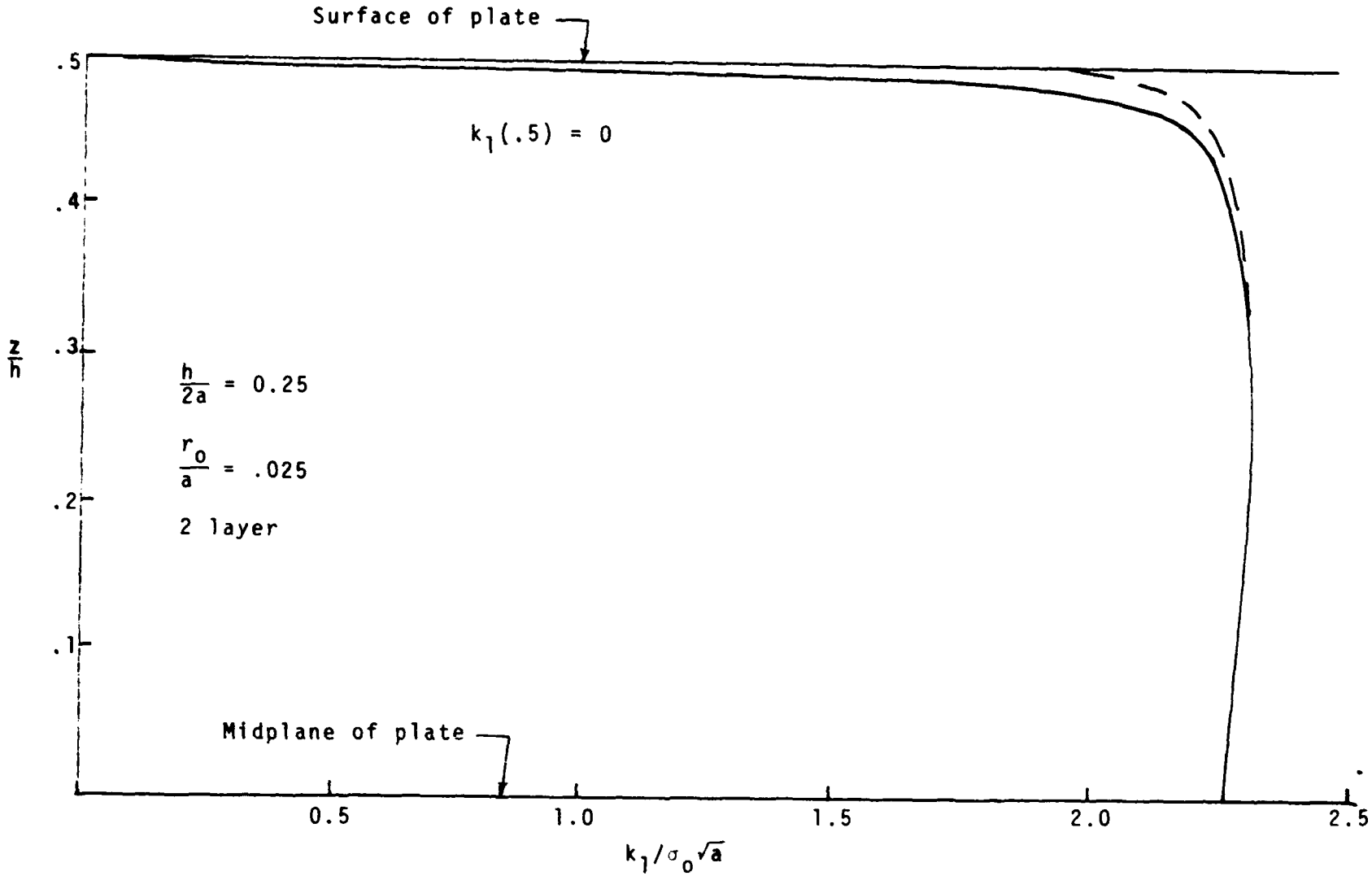

Figure 28 - The influence of the surface constraint on the stress intensity factor variation.

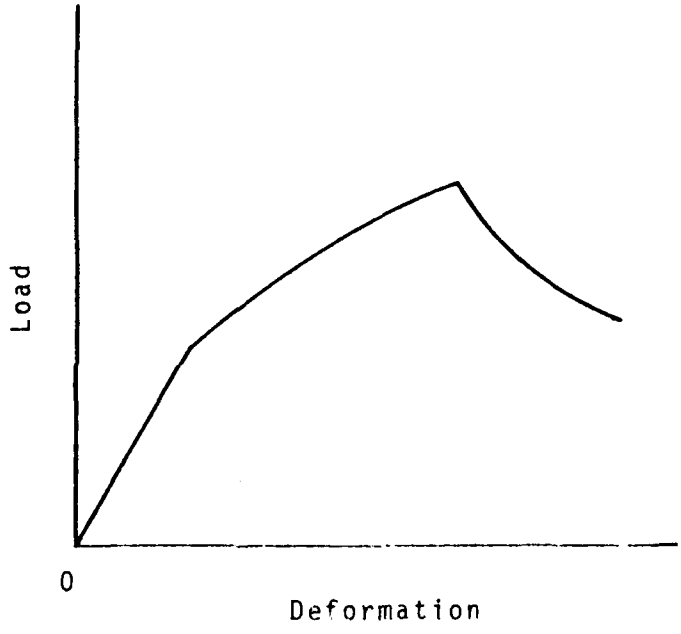

Figure 29 - Load versus deformation curve.

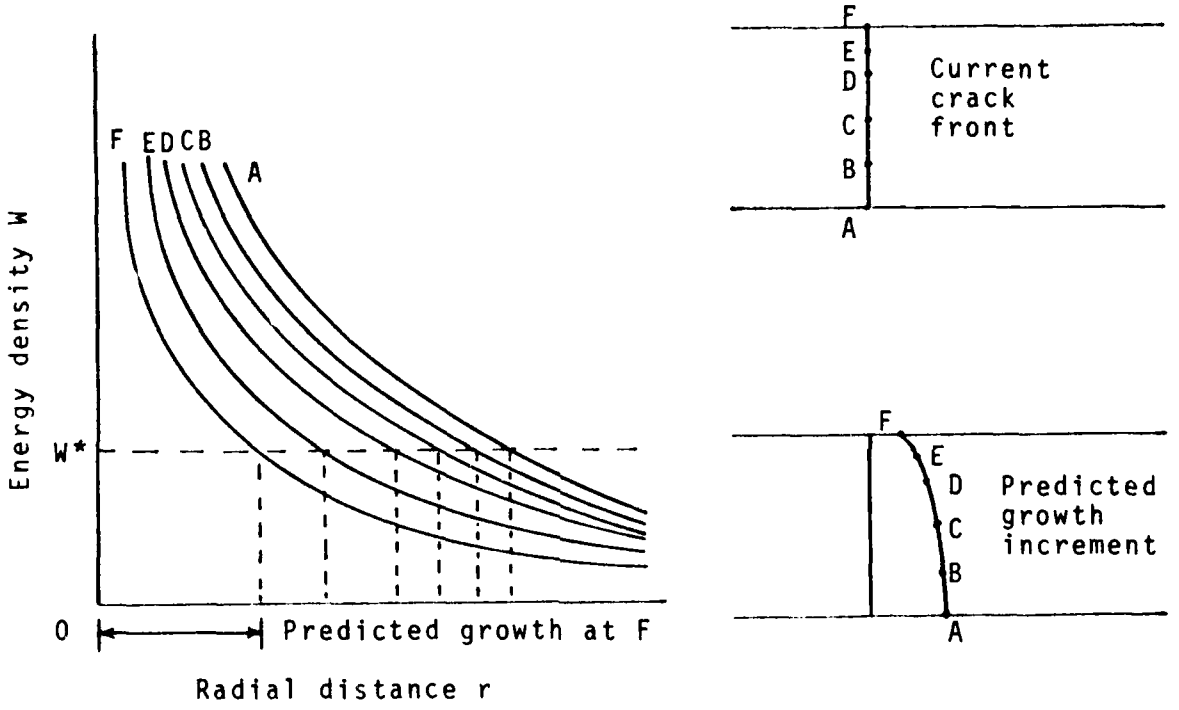

Figure 30 - Growth prediction based on strain energy density

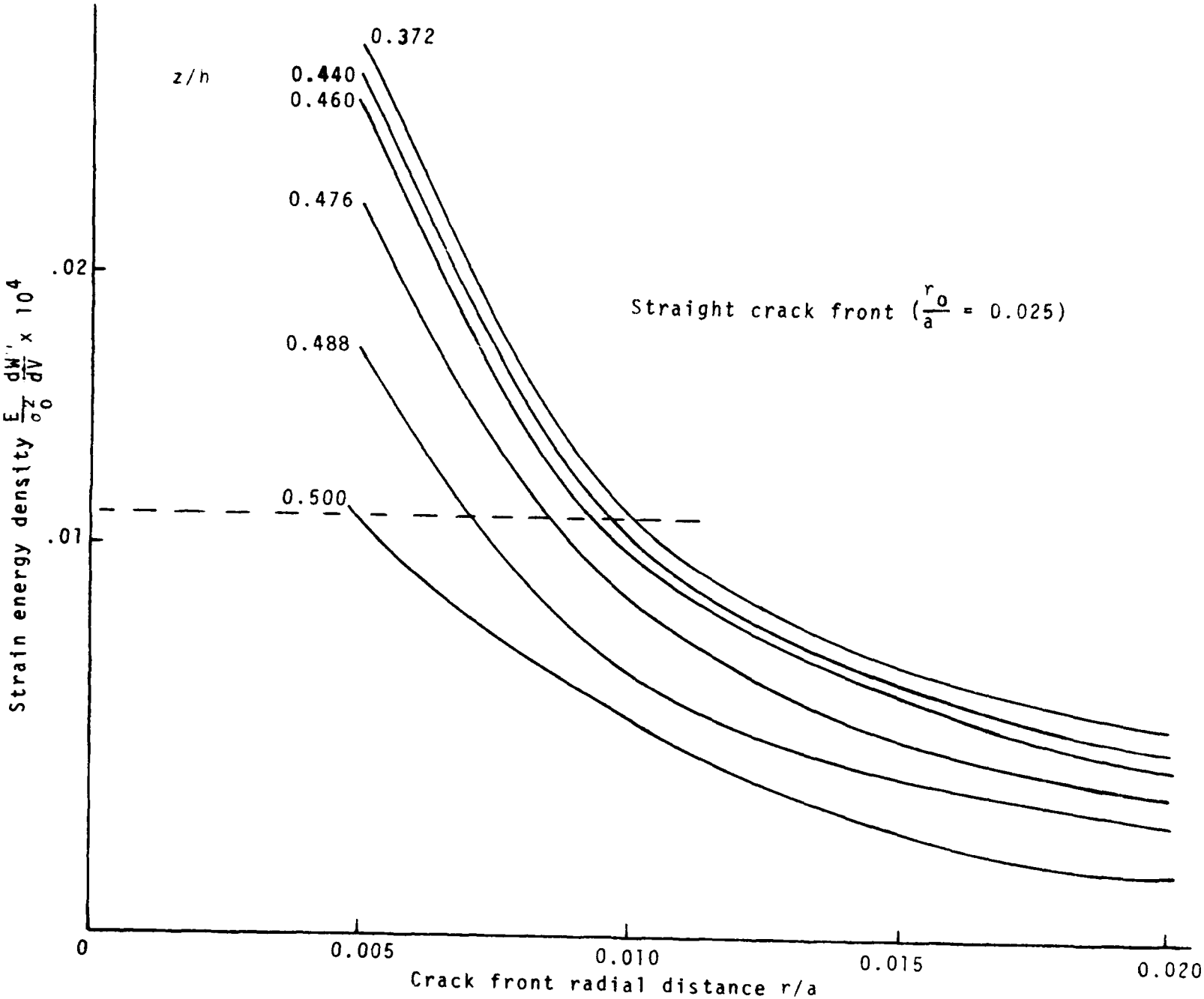

Figure 31 - Strain energy density variation along a straight crack front.

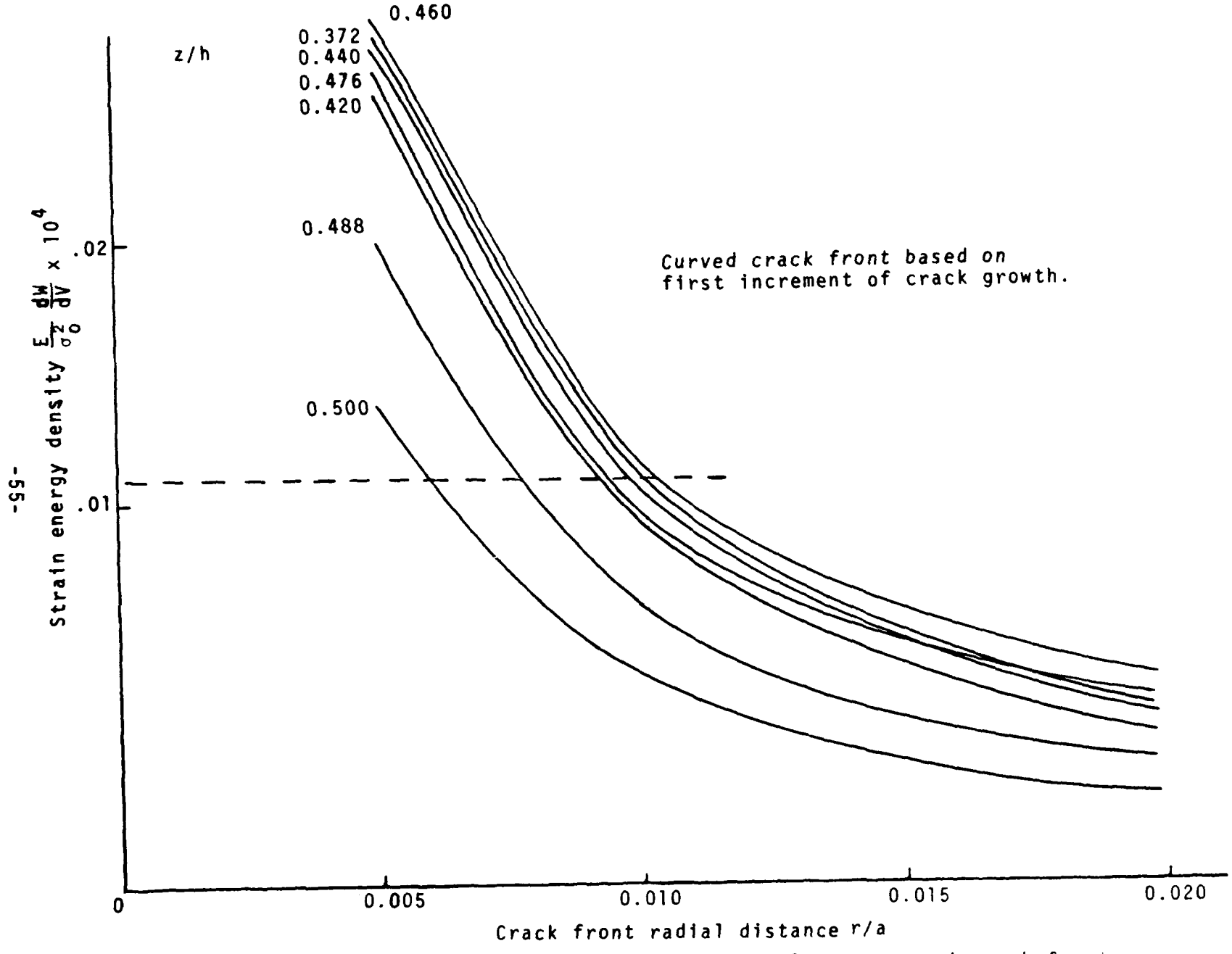

Figure 32 - Strain energy density variation along a curved crack front - first increment at crack growth.

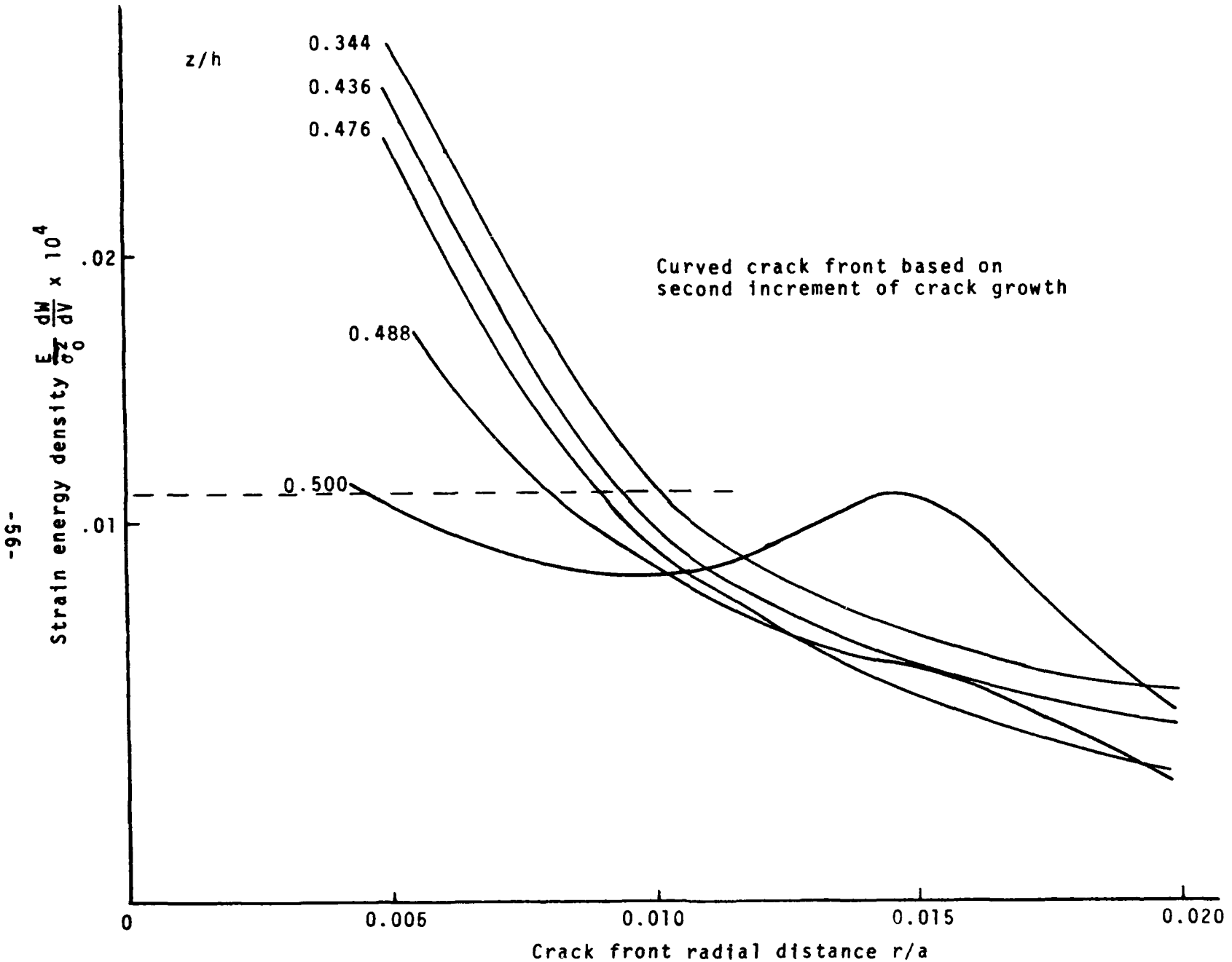

Figure 33 - Strain energy density variation along a curved crack front - second increment of crack growth.

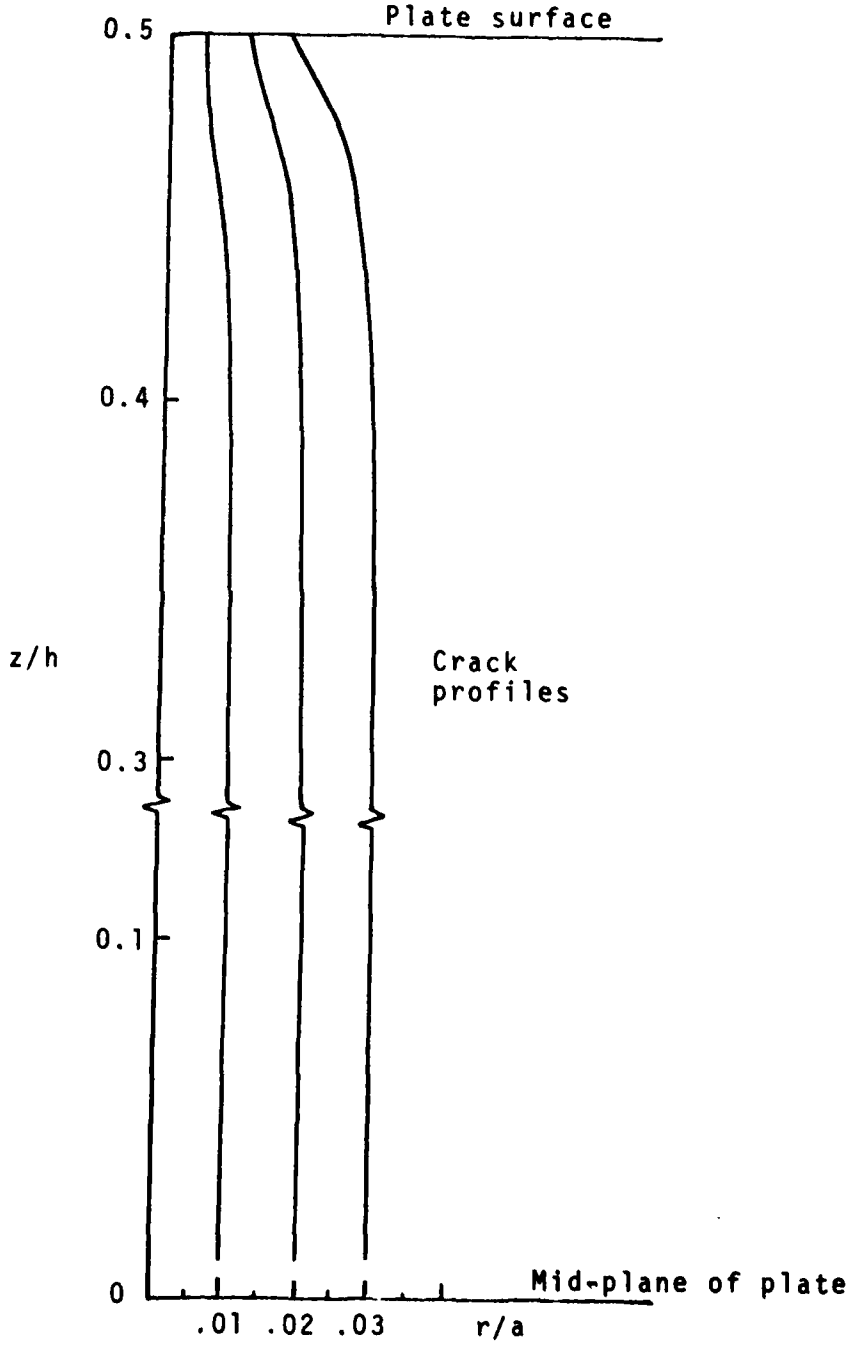

Figure 34 - Predicted increments of crack growth.

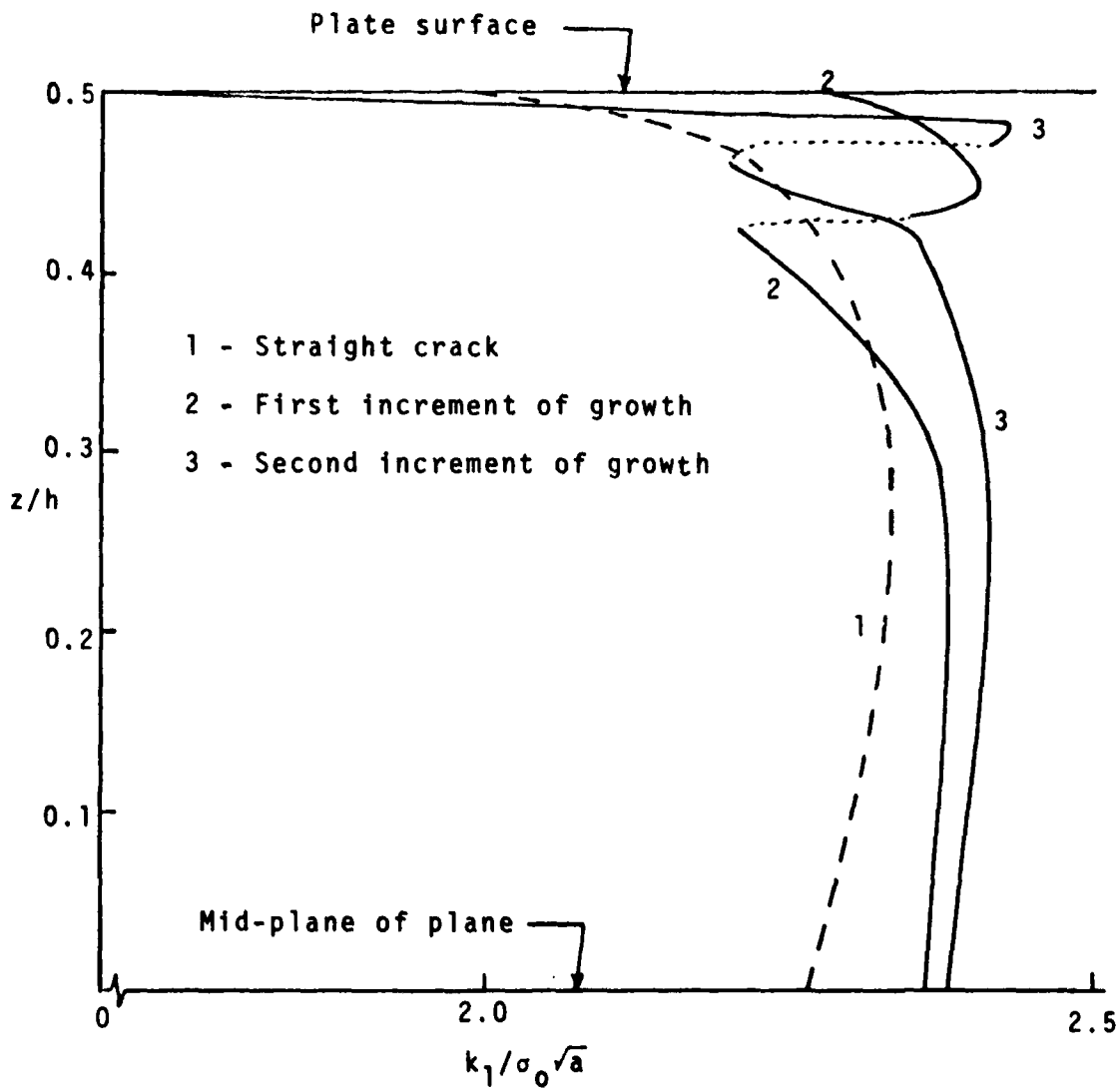

Figure 35 - Variation of stress intensity factor along crack front as it grows.

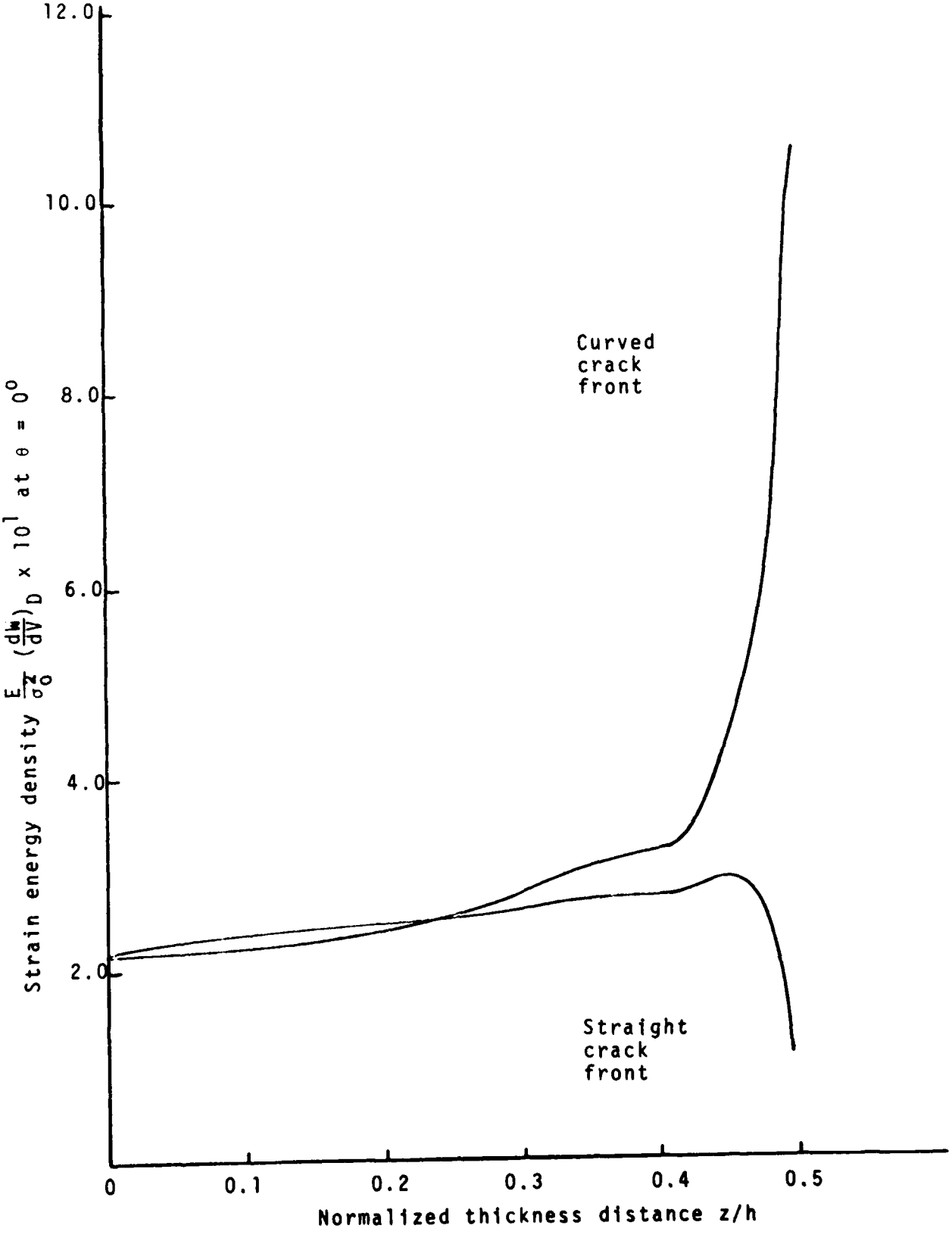

Figure 36 - Variation of strain energy density through plate thickness.

DISTRIBUTION LIST

PART I - GOVERNMENT

Administrative and Liaison Activities

Chief of Naval Research
Department of the Navy
Arlington, Virginia 22217
Attn: Code 439 (3)
461
444

Director
ONR Branch Office
495 Summer Street
Boston, Massachusetts 02210

Director
ONR Branch Office
536 South Clark Street
Chicago, Illinois 60605

Director
Naval Research Laboratory
Attn: Library, Code 2029 (ONRL)
Washington, D.C. 20390 (6)

U.S. Naval Research Laboratory
Attn: Technical Information Division
Washington, D.C. 20390 (6)

Commanding Officer
ONR Branch Office
207 West 24th Street
New York, New York 10011

Director
ONR Branch Office
1030 E. Green Street
Pasadena, California 91101

Defense Documentation Center
Cameron Station
Alexandria, Virginia 22314 (12)

Navy

Chief of Naval Operations
Department of the Navy
Washington, D.C. 20305
Attn: NOP-05F
NOP-506N
NOP-098T

Headquarters
U.S. Marine Corps
Washington, D.C. 20380
Attn: MC-AX-2 (2)
MC-AX-4E2
MC-AAP-3

Commander
Naval Air Systems Command
Department of the Navy
Washington, D.C. 20360
Attn: NAVAIR-320N
NAVAIR-5302
NAVAIR-531
NAVAIR-5311J
NAVAIR-5314
NAVAIR-5325A

Commander
Naval Air Development Center
Warminster, Pennsylvania 18974
Attn: Mr. M. Schulman
Crew Systems Department

Naval Air Development Center
Philadelphia, Pennsylvania 19112
Attn: Dr. E. Hendler
Crew Systems Department

Director
Naval Research Laboratory
Washington, D.C. 20390
Attn: Code 8440 (Dr. F. Rosenthal)

Commanding Officer
Naval Ship Research and Development Center
Bethesda, Maryland 20034
Attn: Code 745 (Mr. B. Whang)

Commanding Officer
Naval Civil Engineering Laboratory
Port Hueneme, California 93041
Attn: Dr. Warren Shaw, Structures Department

Commander
Naval Safety Center
Naval Air Station
Norfolk, Virginia 23511

Capt. Channing L. Ewing Mclusn
Naval Aerospace Medical Research Laboratory
Michoud Assembly Facility
New Orleans, Louisiana 70129

Army

Commanding Officer
U.S. Army Aviation Material Laboratories
Fort Eustis, Virginia 23604
Attn: VDLEU-SS
(Mr. G. T. Singley, III)

Director
U.S. Army Board for Aviation Accident Research
Fort Rucker, Alabama 36360
Attn: BAAR-PP (Mr. J. Haley)

Commanding Officer
U.S. Army Research Office Durham
Attn: Mr. J. J. Murray
CRD-AA-IP
Box CM, Duke Station
Durham, North Carolina 27706

Air Force

Air Force Office of Scientific Research
1400 Wilson Boulevard
Arlington, Virginia 22209
Attn: Mechs. Div.

Commanding Officer
6571st AMRL
Holloman Air Force Base, New Mexico
Attn: Mr. C. C. Gragg

NASA

Mr. C. Kubokawa
N239-3
NASA Ames Research Center
Moffett Field, California 94035

Department of Transportation

Mr. R. F. Chandler
Code AC 119
CAMI, FAA Aeronautical Center
P.O. Box 25082
Oklahoma City, Oklahoma 73123

Mr. H. Spicer
Federal Aviation Administration (DS-41)
800 Independence Avenue, S.W.
Washington, D.C. 20590

Mr. H. Daiutolo
Federal Aviation Administration
NAFEC (NA541)
Atlantic City, New Jersey 08405

Mr. D. Beyer
Federal Aviation Administration (RD-730)
800 Independence Avenue, S.W.
Washington, D.C. 20590

Headquarters
U.S. Coast Guard
400 7th Street, S.W.
Washington, D.C. 20590
Attn: DAT/62
EAE/63
ENE-5/64
IGS-1/61
NMT-t/82
OSR-2/73

Mr. J. G. Viner
Protective Systems Group (RS-12)
Federal Highway Administration
400 7th Street, S.W.
Washington, D.C. 20590

Mr. W. H. Collins
Computer Technology Group (DV-11)
Federal Highway Administration
400 7th Street, S.W.
Washington, D.C. 20590

Mr. Kenneth Batcheller, Chief
Safety Programs Division (RS-20)
Federal Railroad Administration
400 7th Street, S.W.
Washington, D.C. 20590

Mr. E. Ward, Chief
Engineering Research and Development
Division (RT-20)
Federal Railroad Administration
400 7th Street, S.W.
Washington, D.C. 20590

Dr. J. A. Edwards
Associate Administrator for Research
and Development
National Highway Traffic Safety
Administration
400 7th Street, S.W.
Washington, D.C. 20590

Mr. C. D. Ferguson
Office of Crashworthiness (41-40)
National Highway Traffic Safety
Administration
400 7th Street, S.W.
Washington, D.C. 20590

Mr. L. L. Bradford
Office of Vehicle Structures Research
(43-50)
National Highway Traffic Safety
Administration
400 7th Street, S.W.
Washington, D.C. 20590

National Transportation Safety Board
800 Independence Avenue, S.W.
Washington, D.C. 20590
Attn: Mr. A. L. Schmieg, NS-10
Mr. H. L. Morgan, NS-20
Mr. B. C. Doyle, NA-87

Dr. H. E. vonGierke
Aerospace Medical Research
Laboratory
Aerospace Medical Division
Air Force Systems Command
Wright-Patterson Air Force Base,
Ohio 45433

Sal Davis
Fairchild Industries, Inc.
Fairchild Republic Division
Farmingdale, New York 11735

Part II - CONTRACTORS AND OTHER
TECHNICAL COLLABORATORS

Mr. S. P. Desjardins
Dynamic Science
1800 West Deer Valley Drive
Phoenix, Arizona 85027

Dr. A. A. Ezra, Chairman
Department of Mechanical Sciences
and Environmental Engineering
University of Denver
Denver, Colorado 80210

Dr. Albert I. King
Bioengineering Center
Wayne State University
Detroit, Michigan 48202

Dr. R. C. DeHart, Director
Department of Structural Research
Southwest Research Institute
P.O. Drawer 28510
San Antonio, Texas 78284

Professor J. B. Martin
Division of Engineering
Brown University
Providence, Rhode Island 02912

Dr. J. L. Tocher
Boeing Computer Services (72-80)
P.O. Box 24346
Seattle, Washington 98124

Mr. D. G. Harding, Manager
Survivability Staff
Boeing Company - Vertol Division
Philadelphia, Pennsylvania 19142

Dr. H. E. Lindberg, Manager
Engineering Mechanics Program
Stanford Research Institute
Menlo Park, California 94025

Mr. John W. Freyler
Beta Industries, Inc.
2763 Culver Avenue
Dayton, Ohio 45429

Dr. L. E. Hulbert, Chief
Advanced Solid Mechanics Division
505 King Avenue
Columbus, Ohio 43201

Professor George Sih
Department of Mechanics
Lehigh University
Bethlehem, Pennsylvania 18015

Dr. Harold Liebowitz, Dean
School of Engineering and
Applied Science
George Washington University
725 23rd Street
Washington, D.C. 20006

Professor S. B. Dong
University of California
Department of Mechanics
Los Angeles, California 90024

Professor A. J. Durelli
Mechanics Division
The Catholic University of
America
Washington, D.C. 20017

Professor H. H. Bleich
Department of Civil Engineering
Columbia University
Amsterdam & 120th Street
New York, New York 10027

Professor A. M. Freudenthal
George Washington University
School of Engineering and
Applied Science
Washington, D.C. 20006

Professor P. G. Hodge
Department of Mechanics
Illinois Institute of Technology
Chicago, Illinois 60616

Professor D. C. Drucker
Dean of Engineering
University of Illinois
Urbana, Illinois 61801

Professor N. M. Newmark
Department of Civil Engineering
University of Illinois
Urbana, Illinois 61801

Library (Code 0384)
U.S. Naval Postgraduate School
Monterey, California 93940

Dr. Francis Cozzarelli
Division of Interdisciplinary Studies
and Research
School of Engineering
State University of New York
Buffalo, New York 14214

Dr. George Herrmann
Stanford University
Department of Applied Mechanics
Stanford, California 94305

Professor J. D. Achenbach
Technological Institute
Northwestern University
Evanston, Illinois 60201

Professor J. Kempner
Department of Aero. Engrg. and
Applied Mech.
Polytechnic Institute of Brooklyn
333 Jay Street
Brooklyn, New York 11201

Dr. Nicholas J. Hoff
Dept. of Aero. and Astro.
Stanford University
Stanford, California 94305

Professor Norman Jones
Massachusetts Institute of Tech-
nology
Department of Naval Architecture
and Marine Engineering
Cambridge, Massachusetts 02139

Professor Werner Goldsmith
Department of Mechanical
Engineering
Division of Applied Mechanics
University of California
Berkeley, California 94720

Professor W. D. Pilkey
Department of Aerospace Engineering
University of Virginia
Charlottesville, Virginia 22903

Dr. H. N. Abramson
Southwest Research Institute
8500 Culebra Road
San Antonio, Texas 78206

Mr. John Scowcroft
Automobile Manufactures Association
330 New Center Building
Detroit, Michigan 48202

Dr. R. D. Young
Texas Transportation Institute
Texas A & M University
College Station, Texas 77840

Professor J. A. Collins
Mechanical Engineering Department
Arizona State University
Tempe, Arizona 85281

Unclassified

SECURITY CLASSIFICATION OF THIS PAGE (When Data Entered)

REPORT DOCUMENTATION PAGE		READ INSTRUCTIONS BEFORE COMPLETING FORM
1. REPORT NUMBER IFSM-76-76	2. GOVT ACCESSION NO.	3. RECIPIENT'S CATALOG NUMBER
4. TITLE (and Subtitle) Growth Characteristics of a Through Crack in a Plate Specimen,		5. TYPE OF REPORT & PERIOD COVERED Technical Report 6. PERFORMING ORG. REPORT NUMBER
7. AUTHOR(s) P. D. Hilton, G. C. Sih and B. V. Kiefer		8. CONTRACT OR GRANT NUMBER(s) N00014-76-C-0094
9. PERFORMING ORGANIZATION NAME AND ADDRESS Institute of Fracture & Solid Mechanics Lehigh University Bethlehem, Pennsylvania 18015		10. PROGRAM ELEMENT, PROJECT, TASK AREA & WORK UNIT NUMBERS NR-064-562
11. CONTROLLING OFFICE NAME AND ADDRESS Department of the Navy Office of Naval Research Arlington, Virginia 22217		12. REPORT DATE August 1976 13. NUMBER OF PAGES 59
14. MONITORING AGENCY NAME & ADDRESS(if different from Controlling Office)		15. SECURITY CLASS. (of this report) Unclassified 15a. DECLASSIFICATION DOWNGRADING SCHEDULE

16. DISTRIBUTION STATEMENT (of this Report)

Approved for public release; distribution unlimited.

17. DISTRIBUTION STATEMENT (of the abstract entered in Block 20, if different from Report)

18. SUPPLEMENTARY NOTES

19. KEY WORDS (Continue on reverse side if necessary and identify by block number)

Elastic-plastic stress analysis
Minimum strain energy density
Through crack
Stable to unstable transition

20. ABSTRACT (Continue on reverse side if necessary and identify by block number)

This report describes the results of a theoretical study of the problem of a through crack in a tensile plate specimen. Experimental observations indicate that the crack front grows stably in the specimen interior forming a "thumb nail" shape prior to unstable fracture. The amount of interior growth before fracture is found to depend on both geometry (relative specimen thickness), the material properties, and the amount of

DD FORM 1 JAN 73 1473 EDITION OF 1 NOV 65 IS OBSOLETE

Unclassified

SECURITY CLASSIFICATION OF THIS PAGE (When Data Entered)

yielding which tends to delay the onset of rapid fracture.

The goal of this work is to study the interaction of material nonlinearity with geometry and their combined effect on the fracture process. To this end, two-dimensional elastic-plastic and three-dimensional elastic calculations have been performed. The finite element method, specialized to crack problems, is the tool used to obtain numerical results. Predictions on the increments of growth along the crack front are made on the basis of the strain energy density theory that assumes crack trajectory to coincide with path of minimum strain energy density function. Related three-dimensional elastic-plastic calculations are currently being developed to complete the modeling of the ductile fracture process in plate specimens.

INSTRUCTIONS FOR PREPARATION OF REPORT DOCUMENTATION PAGE

RESPONSIBILITY. The controlling DoD office will be *responsible for* completion of the Report Documentation Page, DD Form 1473, in all technical reports prepared by or for DoD organizations.

CLASSIFICATION. Since this Report Documentation Page, DD Form 1473, is used in preparing announcements, bibliographies, and data banks, it should be unclassified if possible. If a classification is required, identify the classified items on the page by the appropriate symbol.

COMPLETION GUIDE

General. Make Blocks 1, 4, 5, 6, 7, 11, 13, 15, and 16 agree with the corresponding information on the report cover. Leave Blocks 2 and 3 blank.

Block 1. Report Number. *Enter the unique alphanumeric report number shown on the cover.*

Block 2. Government Accession No. Leave Blank. This space is for use by the Defense Documentation Center.

Block 3. Recipient's Catalog Number. Leave blank. This space is for the use of the report recipient to assist in future retrieval of the document.

Block 4. Title and Subtitle. Enter the title in all capital letters exactly as it appears on the publication. Titles should be unclassified whenever possible. Write out the English equivalent for Greek letters and mathematical symbols in the title *(see "Abstracting Scientific and Technical Reports of Defense-sponsored RDT E," AD-667 000)*. If the report has a subtitle, this subtitle should follow the main title, be separated by a comma or semicolon if appropriate, and be *initially capitalized*. If a publication has a title in a foreign language, translate the title into English and follow the English translation with the title in the original language. Make every effort to simplify the title before publication.

Block 5. Type of Report and Period Covered. Indicate here whether report is interim, final, etc., and, if applicable, inclusive dates of period covered, such as the life of a contract covered in a final contractor report.

Block 6. Performing Organization Report Number. Only numbers other than the official report number shown in Block 1, such as series numbers for in-house reports or a contractor grantee number assigned by him, will be placed in this space. If no such numbers are used, leave this space blank.

Block 7. Author(s). Include corresponding information from the report cover. Give the name(s) of the author(s) in conventional order *(for example, John R. Doe or, if author prefers, J. Robert Doe)*. In addition, list the affiliation of an author if it differs from that of the performing organization.

Block 8. Contract or Grant Number(s). For a contractor or grantee report, enter the complete contract or grant number(s) under which the work reported was accomplished. Leave blank in in-house reports.

Block 9. Performing Organization Name and Address. For in-house reports enter the name and address, including office symbol, of the performing activity. For contractor or grantee reports enter the name and address of the contractor or grantee who prepared the report and identify the appropriate corporate division, school, laboratory, etc., of the author. List city, state, and ZIP Code.

Block 10. Program Element, Project, Task Area, and Work Unit Numbers. Enter here the number code from the applicable Department of Defense form, such as the DD Form 1498, "Research and Technology Work Unit Summary" or the DD Form 1634, "Research and Development Planning Summary," which identifies the program element, project, task area, and work unit or equivalent under which the work was authorized.

Block 11. Controlling Office Name and Address. Enter the full, official name and address, including office symbol, of the controlling office. *(Equates to funding/sponsoring agency. For definition see DoD Directive 5200.20, "Distribution Statements on Technical Documents.")*

Block 12. Report Date. Enter here the day, month, and year or month and year as shown on the cover.

Block 13. Number of Pages. Enter the total number of pages.

Block 14. Monitoring Agency Name and Address *(if different from Controlling Office)*. For use when the controlling or funding office does not directly administer a project, contract, or grant, but delegates the administrative responsibility to another organization.

Blocks 15 & 15a. Security Classification of the Report; Declassification/Downgrading Schedule of the Report. Enter in 15 the highest classification of the report. *If appropriate, enter* in 15a the declassification/downgrading schedule of the report, using the abbreviations for declassification/downgrading schedules listed in paragraph 4-207 of DoD 5200.1-R.

Block 16. Distribution Statement of the Report. Insert here the applicable distribution statement of the report from DoD Directive 5200.20, "Distribution Statements on Technical Documents."

Block 17. Distribution Statement *(of the abstract entered in Block 20, if different from the distribution statement of the report)*. Insert here the applicable distribution statement of the abstract from DoD Directive 5200.20, "Distribution Statements on Technical Documents."

Block 18. Supplementary Notes. Enter *information not* included elsewhere but useful, such as: Prepared in cooperation with . . . Translation of *(or by)* . . . Presented at conference of . . . To be published in . . .

Block 19. Key Words. Select terms or short phrases that identify the principal subjects covered in the report, and are sufficiently specific and precise to be used as index entries for cataloging, conforming to standard terminology. The DoD "Thesaurus of Engineering and Scientific Terms" *(TEST)*, AD-672 000, can be helpful.

Block 20. Abstract. The abstract should be a brief *(not to exceed 200 words)* factual summary of the most significant information contained in the report. If possible, the abstract of a classified report should be unclassified and the abstract to an unclassified report should consist of publicly-releasable information. If the report contains a significant bibliography or literature survey, mention it here. For information on preparing abstracts see "Abstracting Scientific and Technical Reports of Defense-Sponsored RDT&E," AD-667 000.

GPO 860-885